

Supplementary wavelength calibration methods for SALT/RSS spectropolarimetric observations

Justin Cooper
B.Sc. (Hons)

Submitted in fulfillment of the requirements for the degree
Magister Scientiæ
in the Faculty of Natural and Agricultural Sciences
Department of Physics
University of the Free State
South Africa

Date of submission: March 14, 2024

Supervised by: Prof. B. van Soelen, Department of Physics

Abstract

TODO:

- Done last
- Flow from use of SALT and pipeline and basics of its science implementations into why a more streamlined wavelength calibration is an improvement.
- Give summary of results.
- Aim for a paragraph (~ 600) without going too in-depth into anything specific.
- Brian's comment: Abstract should summarize paper. Include results, conclusions, etc.

Keywords:

TODO:

- Add Keywords \rightarrow look up the astronomy journal keywords
- Look up keywords for pipeline development and data reduction.
- I.E. Polarization: optical, Calibration: wavelength, galaxies: AGN, Blazars, Pipeline, SALT, etc.

Contents

1	Introduction	5
2	Spectropolarimetry and the SALT RSS	7
2.1	Spectroscopy	7
2.1.1	Telescope Optics	7
2.1.2	Slit	8
2.1.3	Collimator	8
2.1.4	Dispersion Element	8
2.1.5	Camera Optics	9
2.1.6	Detector	9
2.1.7	Dispersion of Light	9
2.1.8	Detector and Spectroscopic Calibrations	13
2.2	Polarimetry	19
2.2.1	Polarization	20
2.2.2	Polarization Measurement	22
2.2.3	Polarimetric calibrations	26
2.3	Spectropolarimetry	27
2.3.1	Spectropolarimetric measurement	28
2.3.2	Spectropolarimetric calibrations	29
2.4	The Southern African Large Telescope	29
2.4.1	The primary mirror	30
2.4.2	Tracker and tracking	30
2.4.3	SALT Instrumentation	31
2.5	RSS Spectropolarimetry	33
2.5.1	POLSALT	33
3	Developed Tools	37
3.1	Limitations of POLSALT and the Need for a Supplementary Tool	37
3.2	Wavelength calibrations - Supplementary Tools and IRAF	38
3.2.1	Splitting the POLSALT pre-calibration files	38
3.2.2	IRAF wavelength calibration	39
3.2.3	Joining the wavelength calibrated files	41
3.3	Additional Tools	43
3.3.1	Sky line comparisons	43
3.3.2	Cross correlation	44
3.4	General Reduction Procedure	44
3.4.1	POLSALT Pre-reductions	45
3.4.2	Wavelength Calibration	46

3.4.3	POLSALT Reduction Completion	48
4	Testing	51
5	Science Applications	53
5.1	Application to Spectropolarimetric Standards	53
5.2	Application in publications	53
6	Conclusions	55
	List of Acronyms	57
	Bibliography	59

Chapter 1

Introduction

TODO: Very short intro to Spectroscopy, Polarisation, and Spectropolarisation and their Importance in astronomy

TODO: Problem Statement, VERY IMPORTANT, roughly a sentence but problem thoroughly fleshed out.

TODO: Focus on AGN implications and implementations such as the types of objects and a short history for each type of object, Blazar focus with specification on BL Lacs and FSRQs, the Unified Model, ~~The Blazar sequence~~

TODO: Brian's comment: Highlight importance of polarimetry for understanding emission and how that plays a role in AGN.

TODO: Basics of modelling (Different energy/wavelength ranges used and what the models tell us about emission processes/structure) so that Hester's results can be noted for applications of the pipeline.

TODO: General layout of Dissertation

Chapter 2

Spectropolarimetry and the SALT RSS

This chapter gives an overview of the basics of spectropolarimetry (§ 2.3), and how it functions, following from the principles of both spectroscopy (§ 2.1) and polarimetry (§ 2.2). Further, it is discussed how these techniques are practically implemented for Southern African Large Telescope (SALT) (§ 2.4), using the Robert Stobie Spectrograph (RSS) (§ 2.4.3), and how the spectropolarimetric reduction process is completed (§ 2.5).

2.1 Spectroscopy

Spectroscopy originated in its most basic form with Newton’s examinations of sunlight through a prism (Newton and Innys, 1730) but came to prominence as a field of scientific study with Wollaston’s improvements to the optics elements (Wollaston, 1802), Fraunhofer’s use of a diffraction grating instead of a prism (der Wissenschaften, 1824), and Bunsen and Kirchhoff’s classifications of spectral features to their respective chemical elements (Kirchhoff and Bunsen, 1861).

The simplest spectrometer schematic, as shown in Figure 2.1, consists of incident light collected from the telescope’s optics, labelled A, being focused onto a slit, B, and passed through a collimator, C. The collimator collimates the light allowing a dispersion element, D, to disperse the light into its constituent wavelengths. The resultant spectrum is focused by camera optics, E, onto a focal plane, F. Viewing optics are situated at the focal plane in the case of a spectroscope and a detector is situated at the focal plane in the case of a spectrograph.

2.1.1 Telescope Optics

The telescope optics refers simply to all the components of a telescope necessary to acquire a focal point at the spectrometer entrance, labelled B. The focal point in most traditional telescope designs is fixed relative to the telescope and so the spectrometer may be mounted at that point. In cases where the telescope is designed to have a moving focal point relative to the telescope (see Buckley et al., 2006; Cohen, 2009; Ramsey et al., 1998), the spectrometer, or a signal transfer method such as a fibre feed to the spectrometer, must also move along the telescope’s focal path.

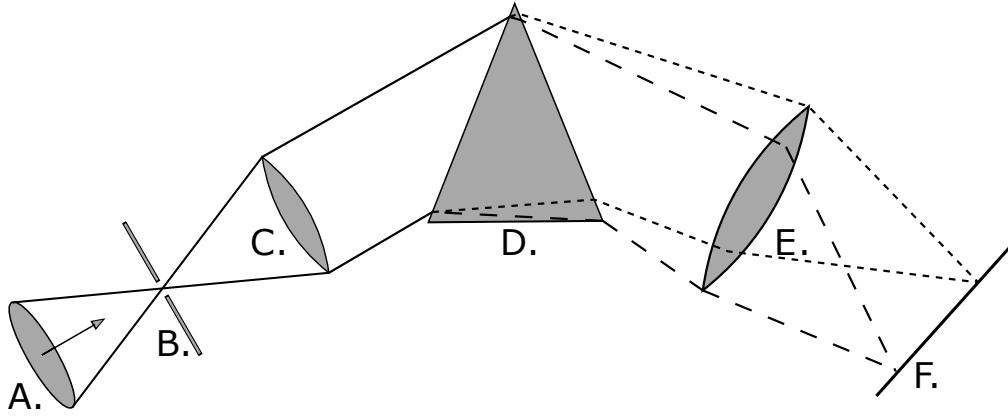


Figure 2.1: Layout depicting the light path through a spectrometer. Diagram adapted from Birney et al. (2006).

2.1.2 Slit

The slit's function is to control the amount of incident light entering a spectrometer and, along with the exposure time of the detector, prevents over-exposures of bright sources on highly sensitive detectors (Tonkin, 2013). If a source is spatially resolvable, or larger than the seeing conditions, the slit additionally acts to spatially limit the source to increase the spectral resolution, resulting in sharper features in the resultant spectrum. Without the slit the spectral resolution would be determined by the projected width of the source on the detector, or the seeing if the source was a star-like point source. Increasing the spectral resolution comes with the trade-off of decreasing the light collected from the source and thus acquiring a less intense resultant spectrum. Multiple spectra may be acquired simultaneously when the slit is positioned such that collinear sources lie along the slit.

The spectrometer is usually situated at the focal point. In cases where this is not feasible due to restrictions, for example restrictions of weight or size, a fibre feed may be situated behind the slit on the telescope. This allows the signal to be routed away from the telescope to a controlled environment with only miniscule losses.

2.1.3 Collimator

The collimators function is to collimate the focused light from the telescope, ensuring that all light rays run parallel before reaching the dispersion element. The focal ratio of the collimator (f_c/D_c , where f refers to the focal length and D refers to the diameter) should ideally match the focal ratio of the telescope (f_T/D_T).

2.1.4 Dispersion Element

Including a dispersion element in the optical path is what defines a spectrometer. As the name suggests, a dispersion element disperses the light incident on it into its constituent wavelengths and produces a spectrum. There are two types of dispersion elements, namely the prism and the diffraction grating, which operate on different principles, as discussed in § 2.1.7.

2.1.5 Camera Optics

The lens functions similarly to that of the telescope's optics but in this case focuses the dispersed light onto a receiver situated at the focal plane. As mentioned previously, an eye piece is fixed to the focal point for a spectroscope while a spectrograph employs a detector.

2.1.6 Detector

The two most prevalent detector types in spectroscopy are the Charged-Coupled Device (CCD) and Complementary Metal-Oxide-Semiconductor (CMOS) detectors. In astronomical spectroscopy however, sources are fainter and exposure times are much longer and so the CCD detectors are by far the preferred detector as their output has a higher-quality and lower-noise when compared to CMOS cameras under the same conditions (Janesick et al., 2006).

The CCD is a detector composed of many thousands of pixels which can store a charge so long as a voltage is maintained across the pixels. Each pixel detects incoming photons using photo-sensitive capacitors through the photoelectric effect and converts the photons to a charge (Buil, 1991). There are also thermal agitation effects which introduce noise to the charge accumulated by a pixel, further discussed in § 2.1.8. Once the exposure is finished the accumulated charge is read column by column, row by row, through an Analog-to-Digital Converter (ADC) which produces a two-dimensional array of 'counts'.

2.1.7 Dispersion of Light

Light can be broken up into its constituent wavelengths through two different physical phenomena, namely dispersion and diffraction, which dispersive elements use to create spectra. Dispersive prisms and diffractive gratings each have their strengths and weaknesses and a wide spectrum of instruments exist which implement either, or both, concepts. Regardless of the specific element, dispersive elements all have a resolving power, R , and an angular dispersion. Generally, while the angular dispersion is a more involved process to determine, the resolving power of a spectrograph can be measured as:

$$R = \frac{\lambda}{FWHM}, \quad (2.1)$$

where λ is the wavelength of an incident monochromatic beam and Full Width at Half Maximum (FWHM) refers to the width of the feature on the detector at half of its maximum intensity.

Prism

The prism operates on the principle that the refractive index of light, n , varies as a function of its wavelength, λ . Prisms were the only dispersive elements available for early spectroscopic studies, but they were not without flaw. The angular dispersion of a prism is given by:

$$\frac{\partial \theta}{\partial \lambda} = \frac{B}{a} \frac{dn}{d\lambda}, \quad (2.2)$$

where θ is the angle at which the refracted light differs from the incident light, λ is the wavelength of the incident light, B is the longest distance the beam would travel through

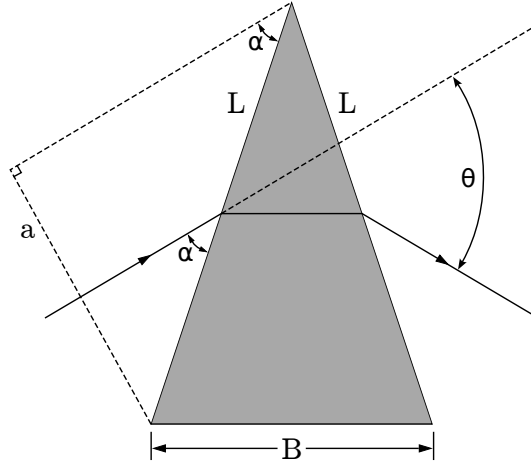


Figure 2.2: Geometry of a prism refracting an incident monochromatic beam at a minimum deviation angle. Diagram adapted from Birney et al. (2006).

the prism. $a = L \sin(\alpha)$ is the maximal beam width that would fit onto a prism with a transmissive surface of length L for a given angle, α , at which a beam would strike the transmissive surface, as shown in Figure 2.2.

The refractive index of a material as a function of its wavelength, $n(\lambda)$, can be approximated by Cauchy's equation:

$$n(\lambda) = A_C + \frac{B_C}{\lambda^2} + \frac{C_C}{\lambda^4} + \dots, \quad (2.3)$$

where A_C, B_C, C_C are the Cauchy coefficients and have known values for certain materials. Cauchy's equation is a much simpler approximation of the refractive index that remains very accurate at visible wavelengths (Jenkins and White, 1976). Taking only the first term of the derivative of the Cauchy equation allows us to approximate the angular dispersion of a prism,

$$\frac{\partial \theta}{\partial \lambda} = -\frac{B}{a} \frac{2B_C}{\lambda^3} \propto -\lambda^{-3}, \quad (2.4)$$

which shows that the angular dispersion of a prism is wavelength dependent and furthermore that longer wavelengths are dispersed less than shorter wavelengths (Birney et al., 2006; Hecht, 2017). The dependence of the angular dispersion, $d\theta/d\lambda$, on the wavelength, λ , is crucial for the formation of a spectrum but this cubic, non-linear, relation results in a non-linear spectrum. Since prisms rely on the refractive index of the material they are made of, they have low angular dispersions.

Multiple prisms can be used to increase the angular dispersion but as the dispersion is non-linear it becomes increasingly more difficult to calibrate. The more material and material boundaries the light must pass through, the more its intensity decreases due to attenuation effects and Fresnel losses. Even so, the transmittance of modern prisms for their selected wavelength range is generally very high due to improved manufacturing methods as well as improved transmitting materials.¹

¹See manufacturers technical specifications, THORLABS, or Edmund Optics for example.

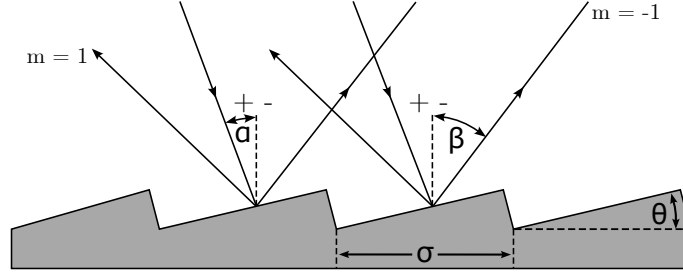


Figure 2.3: Geometry of a reflective blazed grating refracting an incident monochromatic beam. Diagram adapted from Birney et al. (2006).

Diffraction grating

The alternative dispersing element is a diffraction grating, which operates on the principle that as light interacts with a grating where the groove size is comparable to the light's wavelength, the light is dispersed through constructive and destructive interference. This interference results in multiple diffracted beams m , called orders, either side of a central reflected, or transmitted, beam such that $m \in \mathbb{Z}$, where $m = 0$ is the non-dispersed, or reflected, beam.

An example of a reflective blazed grating is illustrated in Figure 2.3. Here a monochromatic beam is incident on the grating at an angle of α from the grating normal. Due to the interference, a diffracted beam of wavelength λ is found at an angle of β from the grating normal. The relation between the incident and diffracted beams is given by the grating equation:

$$m\lambda = \sigma(\sin(\alpha) \pm \sin(\beta)), \quad (2.5)$$

where σ is the groove spacing of the grating and m is the order of the diffracted beam being considered. The grating equation also applies to transmission gratings, though care should be taken for the signs of α and β .

Equation 2.5 also shows that different diffracted beams may share an angle of dispersion for beams not in the same order. The regions of an order that do not overlap with another order are called free spectral ranges. An order-blocking filter may be used to account for the overlaps and increase the free spectral range. A diffraction grating can also be blazed by an angle θ , as illustrated in Figure 2.3. Blazing refers to the fact that the grooves on the surface of the grating are not symmetrical. The asymmetry of the grooves diffracts the incident beam such that most of the beam's intensity is found in a reflected, zeroth order, beam. The wavelength at which a blazed spectrograph is most effective is called the blaze wavelength, λ_b , which is determined by:

$$m\lambda_b = 2\sigma \sin(\theta) \cos(\alpha - \theta), \quad (2.6)$$

where

$$2\theta = \alpha + \beta. \quad (2.7)$$

Taking the derivative of Equation 2.5 with respect to λ while keeping α constant, allows us to determine the angular dispersion of a diffraction grating,

$$\frac{\partial \beta}{\partial \lambda} = \frac{m}{\sigma \cos(\beta)}. \quad (2.8)$$

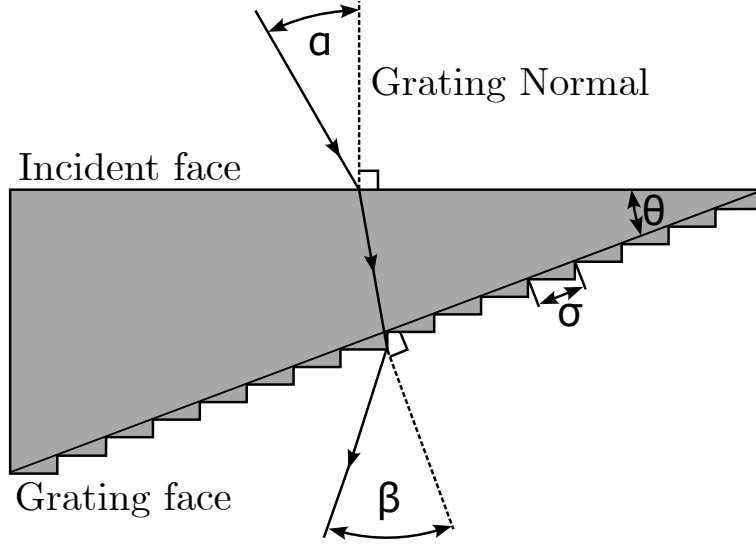


Figure 2.4: Diagram of a grism for an incident monochromatic beam of light and a diffracted beam of order $m = 1$. Diagram adapted from Birney et al. (2006).

Substituting m/σ with the grating equation results in

$$\frac{\partial \beta}{\partial \lambda} = \frac{\sin(\alpha) + \sin(\beta)}{\lambda \cos(\beta)} \propto \lambda^{-1}. \quad (2.9)$$

Similar to the dispersion of a prism, Equation 2.9 shows that the dispersion of a grating is wavelength dependent, but this dependence is only inversely proportional and thus more uniform across a wavelength range than that of a prism. Furthermore, shorter wavelengths are refracted less than longer wavelengths since there is no negative relation between the angular dispersion and the wavelength (Birney et al., 2006; Hecht, 2017).

Alternate Diffraction Elements

As mentioned before, multiple subgroups exist for both dispersive prisms and diffractive gratings. For prisms, along with the single and multiple prism setups mentioned, there also exists grisms and immersed gratings. A grism (Grating Prism), as shown in Figure 2.4, refers to a transmissive grating etched onto one of the transmissive faces of a prism and allows a single camera to capture both spectroscopic and photometric images without needing to be moved, with and without the grism in the path of the beam of light, respectively. An immersed grating refers to a grism modified such that the transmissive grating is coated with reflective material. The primary source of dispersion for both grisms and immersive gratings is the grating and any aberration effects from the prism are negligible in comparison.

Other types of gratings include the Volume Phase Holographic (VPH) grating as well as the echelle grating. The VPH grating consists of a photoresist, which is a light-sensitive material, sandwiched between two glass substrates. Diffraction is possible since the photoresist's refractive index varies near-sinusoidally perpendicularly to the gratings lines, as seen in Figure 2.5. This allows for sharper diffraction orders and low stray light scattering as compared to more traditional gratings but since blazing is not possible the efficiency is decreased. An echelle grating refers to a diffraction grating with higher groove spacing which is optimized for use at high orders. The high order of the diffracted beam



Figure 2.5: Diagram of a VPH grating for an incident monochromatic beam of light. Diagram adapted from Birney et al. (2006).

allows for greater angular dispersion which is most useful when combined with another dispersion element to cross-disperse a spectrum, resulting in a high resolution spectrum.

2.1.8 Detector and Spectroscopic Calibrations

Acquiring a spectrum from observations is more involved than simply reading out the data recorded on the CCD. A raw science image, which is the raw counts of the observed source read from the CCD with no calibrations applied, has on it a combination of useful science data as well as noise. The noise is a combination of random noise introduced through statistical processes and systematic noise introduced through the instrumentation and the observation conditions the source was observed under. This noise causes an uncertainty in the useful data and can be minimized, predominantly by calibrating for the systematic noise, but never fully removed (Howell, 2006).

The dominant source of noise in a raw image is detector noise. CCDs are manufactured to have a small base charge in each pixel, called the ‘bias’ current which allows the readout noise, a type of random noise, to better be sampled. There is also an unintentional additional charge which is linearly proportional to the exposure time and originates from thermal agitation of the CCD material, called the ‘dark’ current. The dark current can be minimized and possibly ignored if the CCD is adequately cooled. These types of noise add to the charge held by a pixel and are thus considered additive.

The CCD is not a perfect detector and the efficiency of it and the optics of the telescope also contribute noise to the image. The efficiency of a CCD is referred to as the Quantum Efficiency, and it is a measure of what percentage of light striking the detector is actually recorded and converted to a charge. The efficiency of the CCD and telescope optics is also wavelength dependent and so the noise that results from them is more complex than that of additive noise. This type of noise is referred to as multiplicative noise.

Additive noise, such as bias and dark currents, is inherent to CCD images, and as such needs to be subtracted out first when performing calibrations. Bias currents can be found by taking a bias image or by adding an overscan region to each image. A bias image is

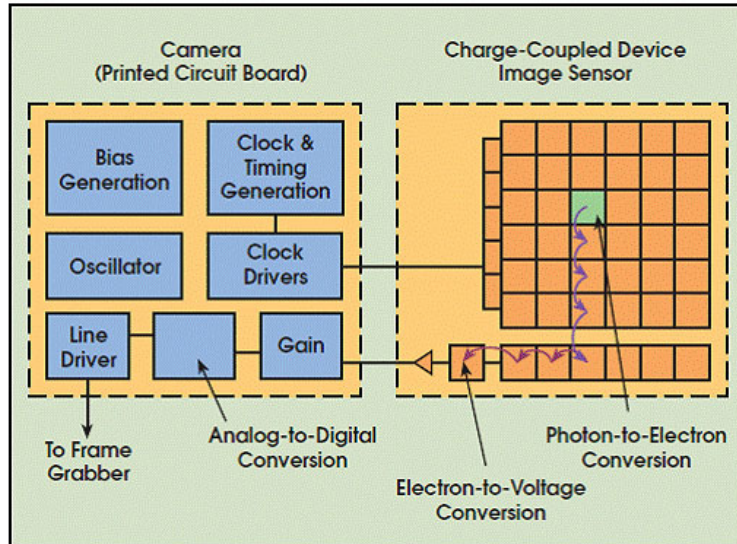


Figure 2.6: Diagram of the inner logic of a CCD. Figure adapted from Litwiller (2001).

an image where the charges on the CCD are reset and then immediately read off without exposing anything on the detector, effectively taking an image with zero exposure time. Alternatively, to save time during an observational run, overscan regions may be added to the images. An overscan region refers to adding a few cycles to the readout of each column of the CCD such that the base current is read out and appended to each image.

Dark currents can be found by taking an image with nothing exposed onto the detector for a certain exposure time. This resultant dark image can then be scaled to the science images exposure time since the dark current should be linearly proportional to exposure time. When the detector is capable of being held at precise temperatures, dark images may be taken over multiple hours during the day to produce a high quality master dark image that may then be scaled and subtracted from all subsequent images.

Next, multiplicative noise, such as a CCD's pixel-to-pixel response, should be accounted for. This pixel-to-pixel response should be uniform across the image and to achieve this an average response may be divided out. The average response is referred to as a 'flat' image or flat-field and may be acquired by observing a uniformly illuminated surface to determine the pixel-to-pixel response.

Dome flats are images taken of a relatively flat surface, usually the inside a telescopes dome, and are used in both photometry and spectroscopy. The surface is uniformly and indirectly illuminated by a projector lamp, ideal for flat-field images. Alternate flat-fielding methods, such as night sky and twilight flats, are available but are suited solely for photometry. Night sky flats are produced from science images containing mostly sky. The science images are combined using the 'mode' statistic which removes any celestial objects at the cost of a low Signal-to-Noise Ratio (S/N) flat-field. Twilight flats are produced from images of the twilight (or dawn) sky. They are taken when the Sun has just set, in the opposite direction, at $\sim 20^\circ$ from zenith and provide a better S/Ns at the cost of careful timing of the images.

A flat-field must be normalized before being used to correct any science images since



Figure 2.7: Example of an arc spectrum for NeAr taken with SALT’s RSS using the PG1800 grating at a grating angle of 34.625° , an articulation angle of 69.258° , and covering a wavelength range of $\sim 5600 - 6900\text{\AA}$. Plot adapted from SALT’s published Longslit Line Atlases, (2023).²

it only acts to account for the pixel-to-pixel response and not for the additive errors. A normalized spectroscopic flat image, $F_\lambda^n(x, y)$, can be calculated as:

$$F_\lambda^n(x, y) = \frac{F_\lambda(x, y) - B(x, y) - (\frac{t_S}{t_D})D(x, y)}{\text{med}_{lp}(F_\lambda(x, y) - B(x, y) - (\frac{t_S}{t_D})D(x, y))}, \quad (2.10)$$

where $F_\lambda(x, y)$ is the non-corrected flat image, $B(x, y)$ is the bias image, $D(x, y)$ is the dark image which is scaled by the exposure time of the science image, t_S , and the dark image, t_D . med_{lp} is a low-pass median filter which smoothes out any rapid changes in the pixel-to-pixel response, removing the illumination contribution.

The calibrated science image, $S_\lambda^*(x, y)$, which accounts for the bias and dark currents as well as the flat fielding can then be calculated as:

$$S_\lambda^*(x, y) = \frac{S_\lambda(x, y) - B(x, y) - (\frac{t_S}{t_D})D(x, y)}{F_\lambda^n(x, y)}. \quad (2.11)$$

When multichannel CCDs are used, which consist of multiple CCDs or a CCD with multiple output amplifiers, additional calibrations, specifically cross-talk corrections and mosaicking, are required. Cross-talk noise refers to contamination that occurs during readout in one channel from another channel with a high signal and occurs because the signals can not be completely isolated from one another. Cross-talk corrections therefore account for this signal contamination between channels being read out at the same time (Freyhammer et al., 2001). Mosaicking is necessary for multichannel CCDs since the digitized signal read out from the detector has no reference of the physical location of the pixel it was detected at. Mosaicking, therefore, correctly orients the data acquired from a multichannel detector so that a single correctly oriented image is produced.

Wavelength Calibration

Finally, since the dispersion element breaks the incident light into its constituent wavelengths non-linearly (§ 2.1.7), the relation between the pixel on a detector and the wavelength of the light incident on it is unknown. Ideally, the spectrometer’s optics would

²NeAr plot sourced from <https://astronomers.salt.ac.za/data/salt-longslit-line-atlas/>

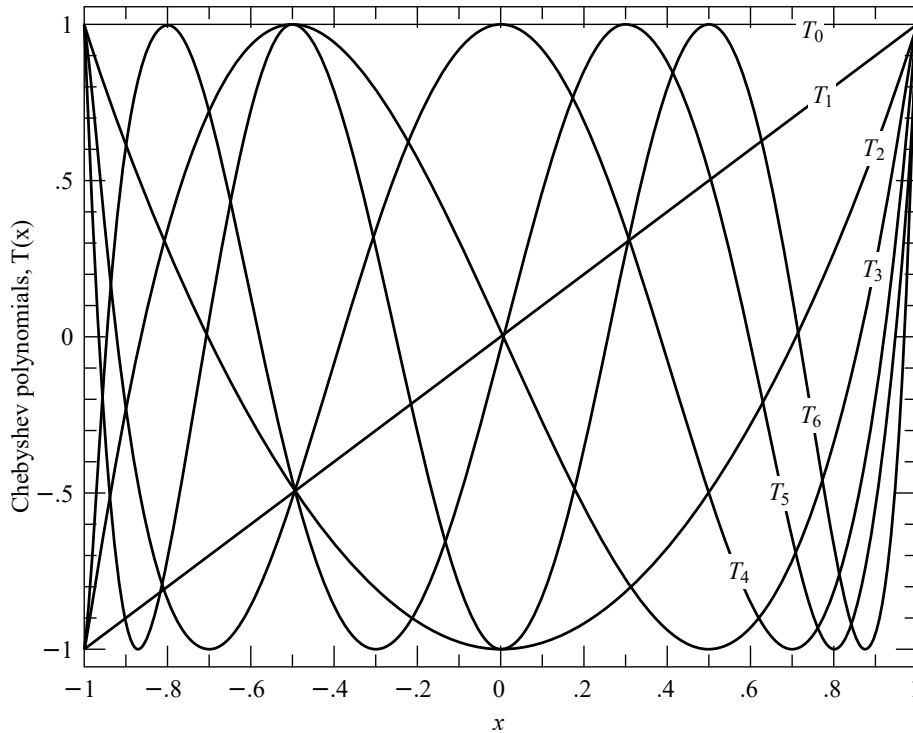


Figure 2.8: The first seven Chebyshev polynomials (T_0 through T_6) as defined by Equation 2.13 over the region $[-1, 1]$ for which they are orthogonal. Plot adapted from (Press et al., 2007) (2023)³

be modelled to produce a reliable pixel to wavelength calibration (see E.g. Liu and Hennelly, 2022), but this becomes increasingly more difficult for spectrometers with complex, non-sedentary, optical paths. Alternatively, a source with well-defined spectral features, with said features evenly populating the wavelength region of interest, such as in Figure 2.7 may be observed. The observed frame is commonly referred to as an ‘arc’ frame, after the arc-lamps used to acquire the spectra, and should be observed alongside the science frames over the course of an observation run. It is important that the arc frame is observed at the same observing conditions and parameters as the science frames since the optical path will vary over the course of an observing run and for different observing parameters, invalidating previously acquired arc frames.

The wavelength calibrations then consist of defining a two-dimensional pixel-to-wavelength conversion function from the arc frame which may later be applied to calibrate the science frames. The two most common approximations for wavelength calibrations are the Chebyshev and Legendre polynomial approximations.

Chebyshev polynomials The Chebyshev polynomials are defined explicitly as:

$$T_n(x) = \cos(n \cos^{-1}(x)), \quad (2.12)$$

or recursively as:

$$\begin{aligned} T_0(x) &= 1, \\ T_1(x) &= x, \quad \text{and} \\ T_n(x) &= 2xT_{n-1}(x) - T_{n-2}(x), \quad \text{for } n > 1, \end{aligned} \quad (2.13)$$

³Excellent resources on Chebyshev and Legendre polynomials are available digitally at www.numerical.recipes/book.

where T is a Chebyshev polynomial of order n .⁴ An important property of Chebyshev polynomials is that they are orthogonal polynomials. This means that the inner product of any two differing Chebyshev polynomials, $T_i(x)$ and $T_j(x)$, over the range $[-1, 1]$ is zero, as shown by:

$$\int_{-1}^1 T_i(x)T_j(x) \frac{1}{\sqrt{1-x^2}} dx = \begin{cases} 0, & i \neq j \\ \pi/2, & i = j \neq 0 \\ \pi, & i = j = 0 \end{cases} \quad (2.14)$$

where $1/\sqrt{1-x^2}$ is the weighting factor for Chebyshev polynomials. This property is important because it means that the coefficients in the Chebyshev polynomial expansion are independent of one another, allowing for a unique solution when approximating an unknown function (Arfken and Weber, 1999; Press et al., 2007).

An approximation, using Chebyshev polynomials, of an unknown wavelength calibration function is given by:

$$f(x) \approx \sum_{i=0}^N c_i T_i(u), \quad (2.15)$$

or

$$F(x, y) \approx \sum_{i=0}^N \sum_{j=0}^M c_{ij} T_i(u) T_j(v), \quad (2.16)$$

for a one- or a two-dimensional wavelength surface function, respectively. Here N and M are the desired x and y orders, and c_i and c_{ij} are the Chebyshev polynomial coefficients (Florinsky and Pankratov, 2015; Leng, 1997). Since the orthogonality property of the Chebyshev polynomials only holds true over the range $[-1, 1]$, the $(x, y) \in ([0, a], [0, b])$ pixel coordinates must be remapped to $u, v \in [-1, 1]$ following the relation:

$$(u, v) = \frac{2(x, y) - a - b}{b - a}. \quad (2.17)$$

The Chebyshev polynomials are more suited for wavelength calibrations than standard polynomials since they are orthogonal and have minima and maxima located at $[-1, 1]$, as seen in Figure 2.8. This means that the Chebyshev approximation is exact when $x = x_n$, where x_n are the positions of the $n - 1$ x -intercepts of $T_N(x)$. These properties greatly minimize the error in the Chebyshev approximation, even at lower order approximations (Arfken and Weber, 1999).

Legendre polynomials Similar to the Chebyshev polynomials, the Legendre polynomials may be defined explicitly as:

$$P_n(x) = \frac{1}{2^n n!} \frac{d^n}{dx^n} (x^2 - 1)^n, \quad (2.18)$$

or recursively as:

$$\begin{aligned} P_0(x) &= 1, \\ P_1(x) &= x, \quad \text{and} \\ P_n(x) &= \frac{2n+1}{n+1} x P_{n-1}(x) - \frac{n}{n+1} P_{n-2}(x), \quad \text{for } n > 1, \end{aligned} \quad (2.19)$$

⁴Chebyshev polynomials are denoted T as a hold-over from the alternate spelling of ‘Tchebycheff’.

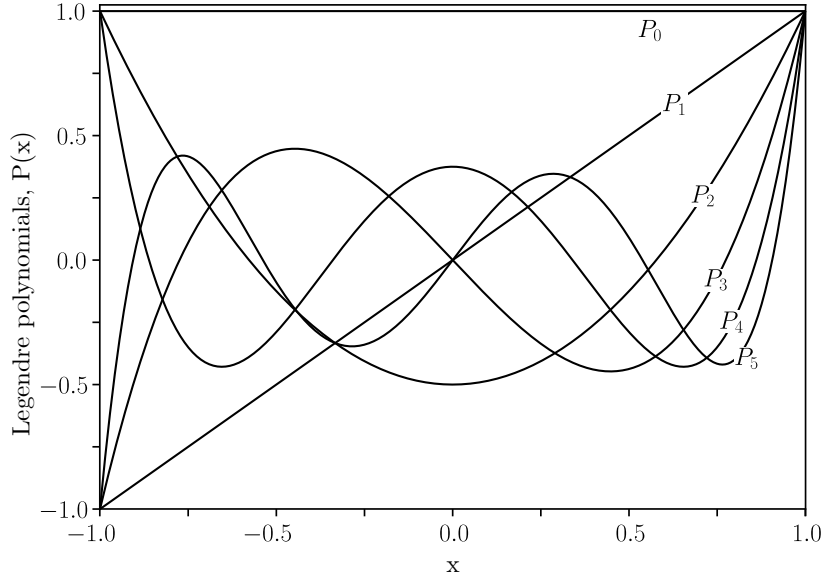


Figure 2.9: The first six Legendre polynomials (P_0 through P_5) as defined by Equation 2.21 over the region $[-1, 1]$ for which they are orthogonal. Plot adapted from Geek3, CC BY-SA 3.0, via Wikimedia Commons (2023).

where P is a Legendre polynomial of order n . Legendre polynomials also hold the property of orthogonality. This means that the inner product of any two differing Legendre polynomials, $P_i(x)$ and $P_j(x)$, over the range $[-1, 1]$ is zero, as shown by:

$$\int_{-1}^1 P_i(x)P_j(x) dx = \begin{cases} 0, & i \neq j \\ \frac{2}{2n+1}, & i = j \end{cases} \quad (2.20)$$

where a weight of 1 is the weighting factor for Legendre polynomials (Dahlquist and Björck, 2003; Press et al., 2007).

An approximation, using Legendre polynomials, of an unknown wavelength calibration function is given by:

$$f(x) \approx \sum_{n=0}^N a_n P_n(u), \quad (2.21)$$

or

$$F(x, y) \approx \sum_{i=0}^N \sum_{j=0}^M a_{ij} P_i(u) P_j(v), \quad (2.22)$$

for a one-dimensional wavelength function or a two-dimensional surface function, respectively. Here N and M are the desired x and y orders, u and v are the same mapping variable as in Equation 2.17, and a_{ij} are the Legendre polynomial coefficients.

Legendre polynomials benefit from having the orthogonality condition with no weight necessary ($w = 1$) which makes their coefficients computationally easier to compute but increases the error in a Legendre approximation when compared to that of the error in a Chebyshev approximation for functions of the same order, N (Ismail, 2005).

Regardless of which method of polynomial approximation is chosen, the polynomials are fit by varying the relevant coefficients using the least squares method. The resultant

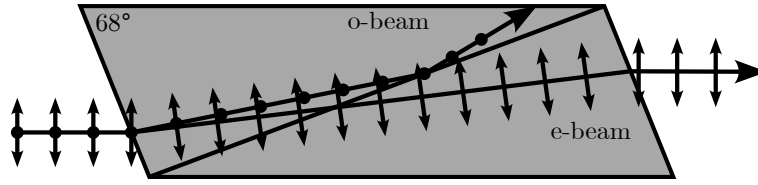


Figure 2.10: Diagram of a Nicol prism for incident non-polarized light. Diagram adapted from Fred the Oyster, CC BY-SA 4.0, via Wikimedia Commons (2023).

minimized function may then be used to convert the science frames from an $(x\text{-pixel}, y\text{-pixel})$ coordinate system to a $(\lambda, y\text{-pixel})$ coordinate system.

2.2 Polarimetry

Both Huygens and Newton came to the conclusion that light demonstrates transversal properties (Huygens, 1690; Newton and Innys, 1730), which was later further investigated and coined as ‘polarization’ by Malus (Malus, 1809). Malus also investigated the polarization effects of multiple materials including some of which were birefringent, such as optical calcite, which he referred to as Iceland spar after Bartholinus’ investigations of the material (Bartholinus, 1670).

Fresnel built on Malus’ work showing that two beams of light, polarized at a right angle to one another, do not interfere, conclusively proving that light is transversal in nature, opposing the widely accepted longitudinal nature of light due to the prevalent belief in the ether. He later went on to correctly describe how polarized light is reflected and refracted at the surface of optical dielectric interfaces, without knowledge of the electromagnetic nature of light. Fresnel’s equations for the reflectance and transmittance, R and T , are defined as:

$$\begin{aligned} R_s &= \left| \frac{Z_2 \cos \theta_i - Z_1 \cos \theta_t}{Z_2 \cos \theta_i + Z_1 \cos \theta_t} \right|^2, \\ R_p &= \left| \frac{Z_2 \cos \theta_t - Z_1 \cos \theta_i}{Z_2 \cos \theta_t + Z_1 \cos \theta_i} \right|^2, \\ T_s &= 1 - R_s, \quad \text{and} \\ T_p &= 1 - R_p, \end{aligned} \tag{2.23}$$

where s and p are the two polarized components of light perpendicular to one another, Z_1 and Z_2 are the impedance of the two media, and θ_i , θ_t , and θ_r are the angles of incidence, transmission, and reflection, respectively (Fresnel, 1870).

Nicol was the first to create a polarizer, aptly named the Nicol prism, where the incident light is split into its two perpendicular polarization components, namely the ordinary and extraordinary beams. Faraday discovered the phenomenon where the polarization plane of light is rotated when under the influence of a magnetic field, known as the Faraday effect. Brewster calculated the angle of incidence, $\theta_B = \arctan n_2/n_1$, at which incident polarized light is perfectly transmitted through a transparent surface, with refractive indexes of n_1 and n_2 , while non-polarized incident light is perfectly polarized when reflected and partially polarized when refracted.

Stokes' work created the first consistent description of polarization and gave us the Stokes parameters which describe an operational approach to measuring polarization (discussed further in § 2.2.1) (Stokes, 1852). Hale was the first to apply polarization to astronomical observations, using a Fresnel rhomb and Nicol prism as a quarter-wave plate and polarizer, respectively (Hale, 1908, 1979). Wollaston also created a prism, similarly named the Wollaston prism, which allowed simultaneous observation of the ordinary and extraordinary beams due to the smaller deviation angle (Wollaston, 1802). Finally, Chandrasekhar's work furthered our understanding of astrophysical polarimetry by explaining the origin of polarization observed in starlight as well as mathematically modeling the polarization of rotating stars, which came to be named Chandrasekhar polarization (Chandrasekhar, 1950).

2.2.1 Polarization

Maxwell's equations for an electromagnetic field propagating through a vacuum are given as:

$$\begin{aligned}\nabla \cdot \mathbf{E} &= 0, \\ \nabla \cdot \mathbf{B} &= 0, \\ \nabla \times \mathbf{E} &= -\frac{1}{c} \frac{\partial \mathbf{B}}{\partial t}, \quad \text{and} \\ \nabla \times \mathbf{B} &= \frac{1}{c} \frac{\partial \mathbf{E}}{\partial t},\end{aligned}\tag{2.24}$$

where \mathbf{E} and \mathbf{B} are the electric and magnetic field vectors, and c is the speed of light. In a right-handed (x, y, z) coordinate system, a non-trivial solution of an electromagnetic wave following Maxwell's Equations propagating along the z -axis, towards a hypothetical observer, is described by:

$$\begin{aligned}\mathbf{E} &= E_x \cos(kz - \omega t + \Phi_x) \hat{\mathbf{x}} + E_y \cos(kz - \omega t + \Phi_y) \hat{\mathbf{y}}, \quad \text{and} \\ \mathbf{B} &= \frac{1}{c} E_y \cos(kz - \omega t + \Phi_y) \hat{\mathbf{x}} + \frac{1}{c} E_x \cos(kz - \omega t + \Phi_x) \hat{\mathbf{y}},\end{aligned}\tag{2.25}$$

where E_x , E_y , Φ_x , and Φ_y are all parameters describing the amplitude and phase of the electric field vector in the (x, y) plane, and with the magnetic field vector proportional and perpendicular to the electric field vector (Griffiths, 2005).

Considering only the electric field component and rewriting Equation 2.25 using complex values allows us to simplify the form of the solution to:

$$\mathbf{E} = \Re(\mathbf{E}_0 e^{-i\omega t}),\tag{2.26}$$

where we only consider the real part of the equation, and where \mathbf{E}_0 is defined as:

$$\mathbf{E}_0 = E_x e^{i\Phi_x} \hat{\mathbf{x}} + E_y e^{i\Phi_y} \hat{\mathbf{y}},\tag{2.27}$$

and is referred to as the polarization vector since it neatly contains the parameters responsible for the polarization properties (Degl'Innocenti, 2014).

For an electric field vector with oscillations in some combination of the x and y axes, the tip of the vector sweeps out an ellipse, as depicted in Figure 2.11. This ellipse is

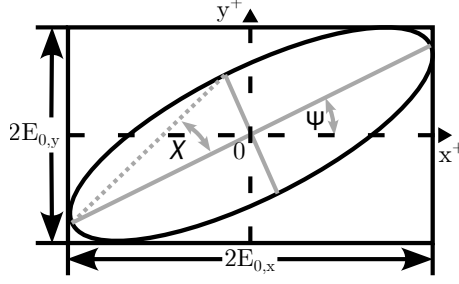


Figure 2.11: The polarization ellipse for an electric field vector propagating through free space. Diagram adapted from Inductiveload, PDM 1.0, via Wikimedia Commons (2023).

referred to as the polarization ellipse and has the form:

$$\left(\frac{\mathbf{E}_x}{\mathbf{E}_{0,x}}\right)^2 + \left(\frac{\mathbf{E}_y}{\mathbf{E}_{0,y}}\right)^2 - \frac{2\mathbf{E}_x\mathbf{E}_y}{\mathbf{E}_{0,x}\mathbf{E}_{0,y}}\cos\Phi = \sin^2\Phi, \quad (2.28)$$

where $\Phi = \Phi_x - \Phi_y$ is the phase difference between the x and y phase parameters. The degree of polarization for the polarization ellipse is related to the eccentricity of the ellipse and the angle at which it is rotated relates to the polarization angle. Since $\mathbf{E}_{0,x}$, $\mathbf{E}_{0,y}$, Φ_x , and Φ_y describe the wave, the polarization ellipse that results from these parameters is fixed as the wave continues to propagate.

Since observations consist of images taken over a desired exposure time, time averaging of Equation 2.28 over the exposure time is necessary. Given the periodical nature and high frequencies of the fields, the time averaging may be found over a single oscillation using:

$$\langle \mathbf{E}_i \mathbf{E}_j \rangle = \lim_{dt \rightarrow \infty} \frac{1}{T} \int_0^T \mathbf{E}_i \mathbf{E}_j dt, \quad \text{for } i, j \in (x, y), \quad (2.29)$$

where T is the total averaging time over the electric field vectors \mathbf{E}_i and \mathbf{E}_j (Collett, 2005). Applying the time averaging to Equation 2.28 and simplifying results in:

$$(E_{0x}^2 + E_{0y}^2)^2 - (E_{0x}^2 - E_{0y}^2)^2 - (2E_x E_y \cos \Phi)^2 = (2E_x E_y \sin \Phi)^2. \quad (2.30)$$

The expressions inside the parentheses can be found through observation and may also be represented as:

$$\mathbf{S} = \begin{pmatrix} S_0 \\ S_1 \\ S_2 \\ S_3 \end{pmatrix} = \begin{pmatrix} I \\ Q \\ U \\ V \end{pmatrix} = \begin{pmatrix} E_{0x}^2 + E_{0y}^2 \\ E_{0x}^2 - E_{0y}^2 \\ 2E_{0x}E_{0y}\cos\Phi \\ 2E_{0x}E_{0y}\sin\Phi \end{pmatrix} \quad (2.31)$$

where S_0 to S_3 are referred to as the Stokes (polarization) parameters. The parameters describe the: S_0 , total intensity (often normalized to 1); S_1 , ratio of the Linear Horizontally Polarized (LHP) to Linear Vertically Polarized (LVP) light; S_2 , ratio of the Linear $+45^\circ$ Polarized (L $+45^\circ$) to Linear -45° Polarized (L -45°) light; and S_3 , ratio of the Right Circularly Polarized (RCP) (clockwise) to Left Circularly Polarized (LCP) (counter-clockwise) light. When the intensity is normalized, the Stokes parameters range from 1 to -1 , based on the dominating component of the parameter (Chandrasekhar, 1950; Stokes, 1852).

From Equations 2.30, 2.31, the polarization parameters are related by:

$$I^2 = Q^2 + U^2 + V^2, \quad (2.32)$$

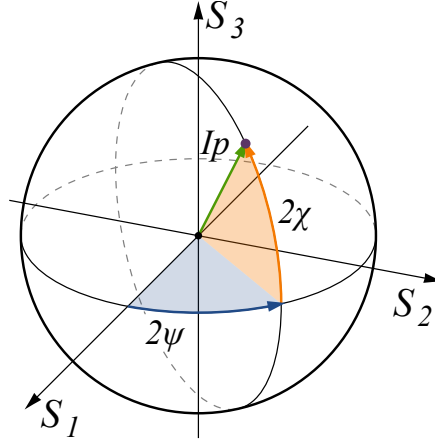


Figure 2.12: The Poincaré sphere describing the polarization properties of a wave-packet propagating through free space. Diagram adapted from Inductiveload, PDM 1.0, via Wikimedia Commons (2023).

for entirely polarized light. Only beams of completely polarized light could be accounted for before Stokes' work on polarization. Using the Stokes parameters, we can now account for partially polarized light such that:

$$I^2 \geq Q^2 + U^2 + V^2, \quad (2.33)$$

where I, Q, U , and V are the normalized polarization parameters.

Similar to the polarization ellipse, the Stokes parameters may be depicted using the Poincaré sphere in spherical coordinates $(IP, 2\Psi, 2\chi)$, such that:

$$\begin{aligned} I &= S_0, \\ P &= \frac{\sqrt{S_1^2 + S_2^2 + S_3^2}}{S_0}, \quad \text{for } 0 \leq P \leq 1, \\ 2\Psi &= \arctan \frac{S_3}{\sqrt{S_1^2 + S_2^2}}, \quad \text{and} \\ 2\chi &= \arctan \frac{S_2}{S_1}, \end{aligned} \quad (2.34)$$

where I denotes the total intensity, P denotes the degree of polarization, or the ratio of polarized to non-polarized light in the wave-packet, χ denotes the polarization angle, and Ψ denotes the ellipticity angle of the polarization ellipse.

2.2.2 Polarization Measurement

Except for polarimetry in the radio-wavelength regime, the polarization of a beam can not be directly measured. The polarization properties may, however, be recovered from the beam through the manipulation of the four parameters given in Equation 2.25. This so-called manipulation is achieved by passing the beam through optical elements which vary the beam for differing amplitudes and phases. These matrix operations may be represented by their corresponding Mueller matrices.

For ideal components, the resultant beam \mathbf{S}' after passing through an optical element is given by $\mathbf{S}' = \mathbf{M}\mathbf{S}$, where \mathbf{S} is the beam incident on the optical element and \mathbf{M}

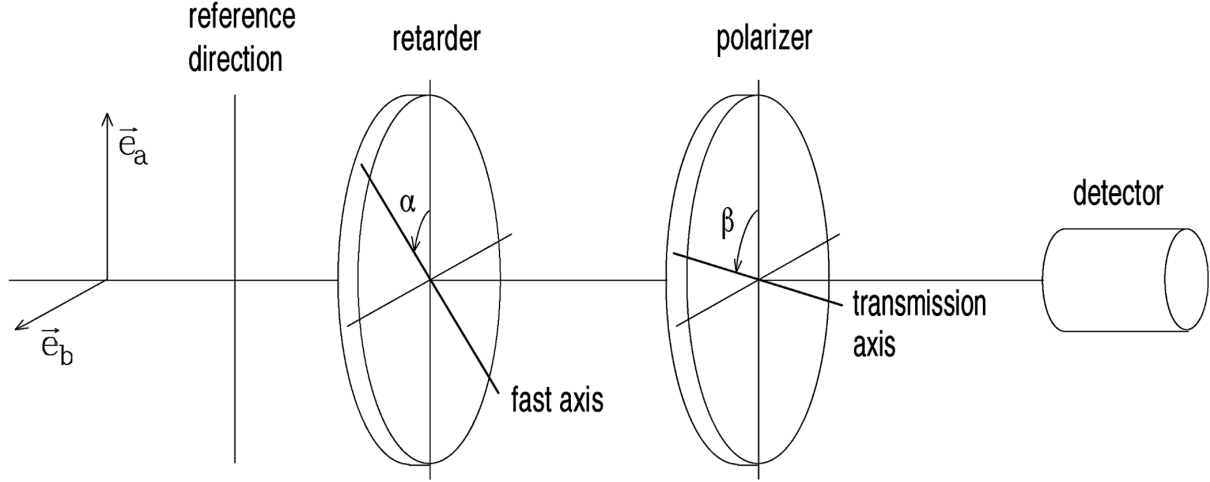


Figure 2.13: Diagram of an ideal polarimeter. Diagram adapted from Degl’Innocenti and Landolfi (2004).

represents the 4×4 Mueller matrix representing the optical element. Mueller matrices are especially useful when dealing with paths through optical elements as they observe the ‘train’ property (Priebe, 1969). This means that an incoming beam \mathbf{S} passing, in order, through elements with known Mueller matrices $(\mathbf{M}_0, \dots, \mathbf{M}_N)$ results in an outgoing beam \mathbf{S}' such that:

$$\mathbf{S}' = \mathbf{M}_N \dots \mathbf{M}_0 \mathbf{S}. \quad (2.35)$$

Some Mueller Matrices are given below with angles related to those in Figure 2.13, measured counter-clockwise in a right-handed coordinate system.

General rotation The Mueller matrix for coordinate space rotations about the origin by an angle θ ,

$$\mathbf{R}(\theta) = \begin{bmatrix} 1 & 0 & 0 & 0 \\ 0 & \cos 2\theta & \sin 2\theta & 0 \\ 0 & -\sin 2\theta & \cos 2\theta & 0 \\ 0 & 0 & 0 & 1 \end{bmatrix}. \quad (2.36)$$

General linear retardance The Mueller matrix for retardance where α is the angle between the incoming vector and fast axis, and δ is the retardance introduced by the retarder,

$$\mathbf{W}(\alpha, \delta) = \begin{bmatrix} 1 & 0 & 0 & 0 \\ 0 & \cos^2 2\alpha + \sin^2 2\alpha \cos \delta & \cos 2\alpha \sin 2\alpha (1 - \cos \delta) & \sin 2\alpha \sin \delta \\ 0 & \cos 2\alpha \sin 2\alpha (1 - \cos \delta) & \cos^2 2\alpha \cos \delta + \sin^2 2\alpha & -\cos 2\alpha \sin \delta \\ 0 & -\sin 2\alpha \sin \delta & \cos 2\alpha \sin \delta & \cos \delta \end{bmatrix}. \quad (2.37)$$

The retarder is often referred to by this retardance, e.g. if the retardance is $\delta = \pi$ or $\pi/2$, the retarder is referred to as a half- or quarter-wave plate, respectively.

General linear polarization The Mueller matrix for linear polarization where β is the angle between the incoming vector and transmission axis,

$$\mathbf{P}(\beta) = \frac{1}{2} \begin{bmatrix} 1 & \cos 2\beta & \sin 2\beta & 0 \\ \cos 2\beta & \cos^2 2\beta & \cos 2\beta \sin 2\beta & 0 \\ \sin 2\beta & \sin 2\beta \cos 2\beta & \sin^2 2\beta & 0 \\ 0 & 0 & 0 & 0 \end{bmatrix}. \quad (2.38)$$

These matrices in combination with Equation 2.35 allow us to describe how the incoming Stokes parameters would change when passing through the various optical elements. For a setup similar to Figure 2.13, the detected Stokes parameters can be described by:

$$S'(\alpha, \beta, \gamma) \propto \frac{1}{2} \{ I + [Q \cos 2\alpha + U \sin 2\alpha] \cos(2\beta - 2\alpha) \\ - [Q \sin 2\alpha + U \cos 2\alpha] \sin(2\beta - 2\alpha) \cos \gamma \\ + V \sin(2\beta - 2\alpha) \sin \gamma \}, \quad (2.39)$$

where the retardance angle, α , polarization angle, β , for a wave plate with a relative phase difference, γ , may be varied to acquire a system of equations that can be solved to retrieve the Stokes polarization parameters (Bagnulo et al., 2009).

Several or more frames taken under differing configurations may be used to reduce a system of equations to extract all four Stokes polarization parameters, but it is possible to extract the I , Q and U polarization parameters using only four frames, or two dual-beam frames, for well-chosen configurations and assuming ideal components. This ideal configuration varies the retarder angle such that $\Delta\alpha = \pi/8$ while keeping the polarizer stationary. More frames for additional retarder angles are advisable and often necessary, however, as they correct for any differences in sensitivity, such as may arise in a polarized flat field and which is further discussed in § 2.2.3 (Patat and Romaniello, 2006).

From Equation 2.39 we see that the linear retarder element is the driving element of a polarizer as the first three Stokes parameters (S_{0-2} , or I , Q , and U) may be found by changing only the angle of retardance, α .

Wave plates Wave plates, also commonly referred to as retarders, are generally made from optically transparent birefringent crystals. A wave plate has a fast and slow axis, which are perpendicular to one another and both perpendicular to an incident beam. Due to the birefringence of the wave plate medium, the phase velocity of the beam polarized parallel to the fast axis, namely the extraordinary beam, slightly increases while that of the beam polarized parallel to the slow axis, namely the ordinary beam, remains unaffected. This difference in the perpendicular component's phase velocities introduces a relative phase difference between the two beams, γ , which is given by:

$$\gamma = \frac{2\pi\Delta n L}{\lambda_0} \quad (2.40)$$

where Δn and L refer to the birefringence and thickness of the wave plate medium, respectively, and λ_0 refers to the vacuum wavelength of the beam (Hecht, 2017).

This relative phase difference determines the name of the wave plate, such that the $\gamma = m(\pi/2)$ and $\gamma = m(\pi/4)$ phase differences, for $m \in \mathbb{Z}^+$, refer to the half- and quarter-wave plates (which are the most common wave plate phases), respectively. Phase differences with an integer multiple of one another relate to the same phase difference and are referred to as multiple-order wave plates, while wave plates with a phase difference less than an integer multiple are referred to as zero-order wave plates. Several multiple-order wave plates can be combined by alternatively aligning the fast axis of one to the slow axis of another to create a compound zero-order wave plate (Hale and Day, 1988).

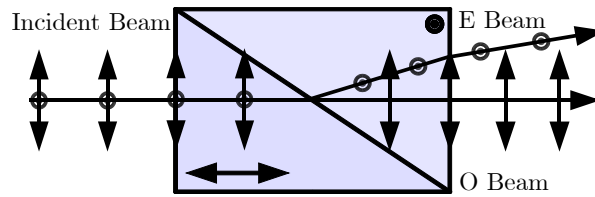


Figure 2.14: Diagram of a Rochon prism. Included in the diagram are the optical axes of the differing sections of the birefringent material as well as polarizing directions of the incident beam, denoted using the \leftrightarrow and \odot symbols, for the O - and E -beams, respectively. Figure adapted from ChrisHodgesUK, CC BY-SA 3.0, via Wikimedia Commons (2023).

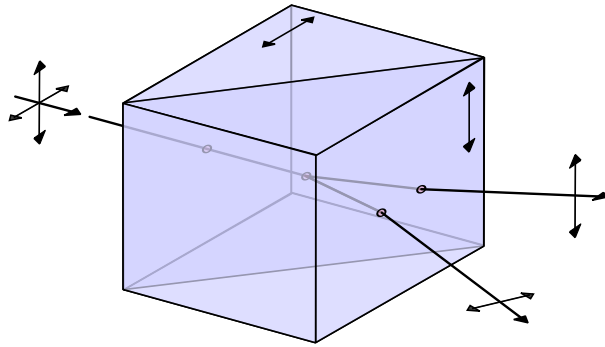


Figure 2.15: Diagram of a Wollaston prism. Included in the diagram are the optical axes of the differing sections of the birefringent material as well as polarizing directions of the incident beam, denoted using the \leftrightarrow and \updownarrow symbols, for the O - and E -beams, respectively. Diagram adapted from fgalore, CC BY-SA 3.0, via Wikimedia Commons (2023).

Polarizers Polarizers are typically made from two prisms, of a birefringent material, cemented together with an optically transparent adhesive. The actual effect of separating the perpendicular polarization components is achieved using varying effects, namely through:

- absorption of one of the polarized components, such as in Polaroid polarizing filters,
- total internal reflection of a single polarized component, such as in a Nicol prism (Figure 2.10),
- Refraction of a single polarized component, such as in a Rochon prism (Figure 2.14), or
- Refraction of both polarization components in differing directions, such as in a Wollaston prism (Figure 2.15).

Wollaston prisms The Wollaston prism consists of two right-angle prisms consisting of a birefringent monoaxial material, cemented together with an optically transparent adhesive along their hypotenuses with their optical axes orthogonal, as seen in Figure 2.15. The Wollaston prism is a common optical polarizing element in astrophysical polarimetry which separates an incident beam into two linearly polarized O - and E -beams, orthogonal to one another, and deviated from their common axis equally. The deviation angle of the polarized beams is determined by the wedge angle which is defined as the angle from the common hypotenuse to that of the outer transmission face of either prism.

Wollaston prisms benefit over simpler elements (such as those listed in the polarizer paragraph) since a single frame allows for the observation of both orthogonal polarization components. This halves the observational time required to collect enough data to

calculate the Stokes parameters, at the cost of an increase in calibration and reduction difficulty (Simon, 1986).

2.2.3 Polarimetric calibrations

The raw science images acquired during polarimetric observations contain a combination of useful science data as well as noise, similar to § 2.1.8. Corrections and calibrations related to the detector remain unchanged from those described in § 2.1.8, while those related to correcting for the optical elements relate to corrections for spurious polarization effects.

Flat Fielding

Once the CCD calibrations have been completed, the polarization intrinsic to the optical elements needs to be accounted for such that the pixel-to-pixel response is made uniform. Flat-fielding is, once again, used to correct for this. The flats taken for polarimetry, however, introduce an additional challenge as the targets for conventional flats are polarized, such as twilight and dome flats which are polarized by light scattering in the atmosphere and the reflective surface of the dome, respectively.

If no unpolarized flat images can be taken for flat field calibrations then, when possible due to the polarimeter design, the wave plate may be constantly rotated to act as a depolarizing element; this is effective so long as the wave plate rotation period is much faster than the flat’s exposure time. Alternatively, polarized flats may be taken at the same set of half-wave plate angles used for science observations and averaged together to achieve a similar depolarizing effect.

Observing additional ‘redundant’ exposures for the science and flat images increases the depolarizing effect up to the maximum of 16 half-wave plate positions, where exposures with a half-wave plate angle differing by $\pi/4$ from another are considered redundant due to the *O*- and *E*-beams swapping between the related exposures.

Increasing the amount of redundant observations proportionally increases the time needed to observe all the exposures, which in turn introduces time-dependent effects such as fringing or intensity variations of the flat source. As such, a middle ground must be found for the amount of redundant frames observed. (Patat and Romaniello, 2006; Peinado et al., 2010).

Dual-beam Extraction and Alignment

After calibrations for the CCD and light path are accounted for, the *O*- and *E*-beams can be extracted and further reduced. The extraction depends heavily on the layout of the polarimeter but often a simple cropping of the differing sections is enough to separate the two images.

After extracting the *O*- and *E*-beams for a specific half-wave plate angle, the images need to be aligned such that the sources present in them overlap. The Wollaston prism needs to be corrected for as it introduces a beam deviation which differs across both images. The aligning of the *O*- and *E*-beams is crucial as the comparison of the dual images is what allows for the calculation of the polarization properties.

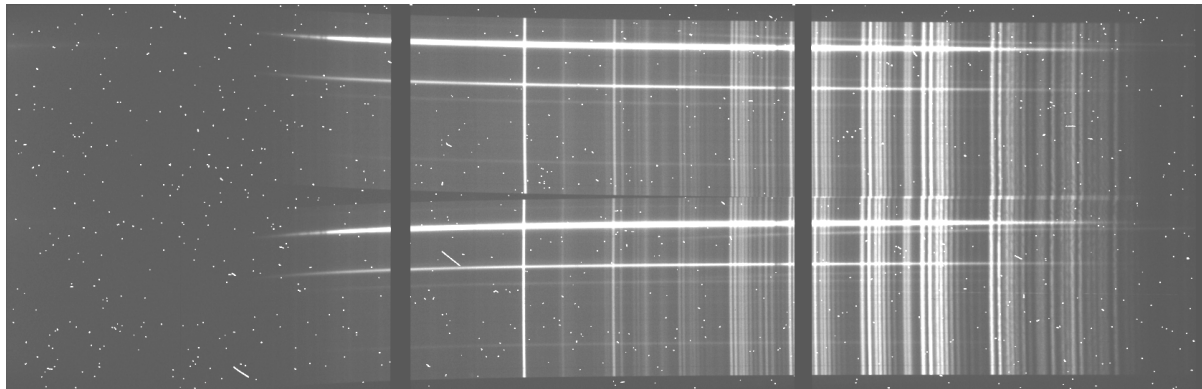


Figure 2.16: A spectropolarimetric target exposure as observed by the SALT RSS in spectropolarimetry mode.

Sky Subtraction

The polarization introduced by the sky introduces a difference in the intensity of the background sky and needs to be removed as it will influence the polarization results of the target source. Thankfully, the background polarization is an additive type of noise and may be subtracted out across the frames. This subtraction is done independently for both beams in a frame and for each frame since the background intensity of all observed polarimetric beams will differ based on the observational parameters.

2.3 Spectropolarimetry

As the name suggests, spectropolarimetry is the measurement of the polarization of light for a chosen spectral range and provides polarimetric results as a function of wavelength. As spectropolarimetry is so closely reliant on both spectroscopy and polarimetry, advancements in spectropolarimeters have always been gated by the advancements of spectrometers and polarimeters (as described in § 2.1, 2.2).

The most notable historical contributions of spectropolarimetry are those of spectropolarimetric studies instead of instrumental developments. Spectropolarimetry provides further insights into a materials physical structure, chemical composition, and magnetic field, allowing spectropolarimetry to be useful across multiple disciplines. In astronomy in particular, spectropolarimetry has been used to study the magnetic field, chemical composition, and underlying structure and emission processes of multiple types of celestial objects (see for example Antonucci and Miller, 1985; Donati et al., 1997; Wang and Wheeler, 2008).

Along with common points of consideration when developing any instrumentation for observational astronomy, such as resolution and sensitivity, spectropolarimeters need to consider the spectral response of the polarimetric components as well as the polarization response of the spectroscopic components as both are simultaneously in the light-path during observations and have noticeable affects on one another. Time is another constraint for spectropolarimetry as the incident light is separated both by wavelength and by polarization states. This division of the incident light results in increased exposure times of not only observations of targets but also observations needed for calibrations, both of which are time-dependent.

Figure 2.16 illustrates a typical science image taken with a spectropolarimeter. The image contains the O - and E -beams which are both dispersed into their spectra. Spectropolarimetric results are acquired from measurements and calibrations of these images alongside any necessary calibration images.

2.3.1 Spectropolarimetric measurement

The derived relations given in § 2.2.1, such as the Stokes parameters, are valid for both polarimetry and spectropolarimetry due to the time averaging, which accounts for temporal variations and permits partially polarized incident beams, and the achromatic nature of the polarization calculations.

For linear spectropolarimetry with half-wave plate angles of θ_i , an exposure measures the wavelength dependent intensities of the O - and E -beams, $I'_O(\lambda)$ and $I'_E(\lambda)$, respectively. The O - and E -beam intensities thus relate to the Stokes parameters following:

$$\begin{aligned} I'_{O,i}(\lambda) &= \frac{1}{2}[I + Q \cos(4\theta_i) + U \sin(4\theta_i)], \\ I'_{E,i}(\lambda) &= \frac{1}{2}[I - Q \cos(4\theta_i) - U \sin(4\theta_i)]. \end{aligned} \quad (2.41)$$

At least two exposures are needed to solve for the I , Q , and U polarization parameters since two equations arise from a single exposure of a dual-beam configuration and at least four linear equations are required to solve for three variables in a system of linear equations.

The first Stokes parameter, I , may be recovered for each dual-beam exposure as

$$I(\lambda) = f_{O,i}(\lambda) + f_{E,i}(\lambda). \quad (2.42)$$

Next, the second and third Stokes parameters, Q and U , are found by first defining the normalized difference in relative intensities as

$$F_i(\lambda) \equiv \frac{f_{O,i}(\lambda) - f_{E,i}(\lambda)}{f_{O,i}(\lambda) + f_{E,i}(\lambda)} \quad (2.43)$$

which then allows Equation 2.41 to be written in terms of the normalized Stokes parameters, $\bar{Q} = Q/I$ and $\bar{U} = U/I$, or, alternatively, the degree of polarization, P , and polarization angle, χ :

$$F_i(\lambda) = \bar{Q}(\lambda) \cos(4\theta_i) + \bar{U}(\lambda) \sin(4\theta_i) = P \cos(4\theta_i - 2\chi). \quad (2.44)$$

The optimal change in waveplate angle is $\Delta\theta = \pi/8$ as it allows the normalized Stokes polarization parameters to be written as:

$$\begin{aligned} \bar{Q}(\lambda) &= \frac{2}{N} \sum_{i=0}^{N-1} F_i(\lambda) \cos\left(\frac{\pi}{2}i\right) \\ \bar{U}(\lambda) &= \frac{2}{N} \sum_{i=0}^{N-1} F_i(\lambda) \sin\left(\frac{\pi}{2}i\right) \end{aligned} \quad (2.45)$$

where N is the amount of exposures taken, limited such that $N \in [2, 16]$, and F_i is the normalized difference in relative intensities for the i^{th} exposure (Patat and Romaniello, 2006).

The desired degree of polarization as well as the polarization angle for linear spectropolarimetry is calculated as:

$$\begin{aligned} P &= \sqrt{\bar{Q}^2 + \bar{U}^2} \\ \chi &= \frac{1}{2} \arctan \frac{\bar{U}}{\bar{Q}} \end{aligned} \quad (2.46)$$

which is derived from Equations 2.34 or by solving a system of linear equations of Equation 2.44 (Degl’Innocenti et al., 2006; Keller, 2002).

2.3.2 Spectropolarimetric calibrations

The calibrations necessary for the measurement to take place are, as always, seemingly more involved than the calculation of the results themselves. As spectropolarimetry is an amalgamation of spectroscopy and polarimetry, it naturally follows that the calibrations necessary are a combination of both calibrations, as discussed in § 2.1.8, 2.2.3. Even though the spectrometer and polarizer components both have an effect on an incident beam following the light-path through the spectropolarimeter, the calibrations procedures for both components remain mostly independent of one another and as such need not be repeated here.

Spectropolarimetric calibrations are, however, more involved when compared to the previous calibration discussions as minor deviations in the calibrations across the spectra and the polarized beam may compound, resulting in poor S/N’s for the spectropolarimetric results. Generally, more exposures over longer timespans are required to acquire enough redundancy and signal for the calculation of the Stokes parameters on top of the time necessary for calibrations to be completed. It should therefore be noted just how important the wavelength and image alignment calibrations are when dealing with spectropolarimetry.

2.4 The Southern African Large Telescope

SALT is a 10 m class optical/near-infrared telescope situated at the South African Astronomical Observatory (SAAO) field station near Sutherland, South Africa (Burgh et al., 2003). The operational design was based off of the Hobby-Eberly Telescope (HET) situated at McDonald Observatory, Texas, which limits the pointing of the telescope’s primary mirror to a fixed elevation (37° from zenith in the case of SALT) while still allowing for full azimuthal rotation (Ramsey et al., 1998). Both SALT and HET utilize a spherical primary mirror which is stationary during observations and a tracker housing most of the instrumentation that tracks the primary mirrors spherically shaped focal path. Figure 2.17 depicts SALT’s tracker (top left), supporting structure, and primary mirror (bottom right).

⁵http://pysalt.salt.ac.za/proposal_calls/current/ProposalCall.html

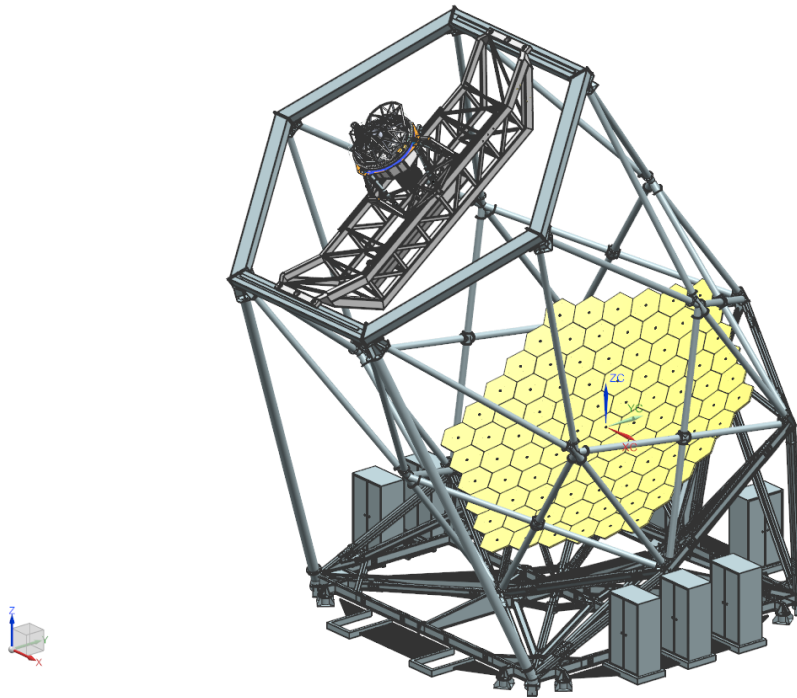


Figure 2.17: The tracker, supporting structure, and primary mirror of SALT. Figure adapted from the SALT call for proposals (2022)⁵

2.4.1 The primary mirror

The primary mirror is composed of 91 individual 1 m hexagonal mirrors which together form an 11 m segmented spherical mirror. Each mirror segment can be adjusted by actuators allowing the individual mirrors to approximate a single monolithic spherical mirror. The fixed elevation means that SALT's primary mirror has a fixed gravity vector allowing for a lighter, cost-effective supporting structure when compared to those of a more traditional altitude-azimuthal mount but with the trade-off that the control mechanism and tracking has increased complexity (Buckley et al., 2006).

2.4.2 Tracker and tracking

During observations the primary mirror is stationary and the tracker tracks celestial objects across the sky by moving along the primary focus. The tracker is capable of 6 degrees of freedom with an accuracy of $5 \mu\text{m}$ and is capable of tracking $\pm 6^\circ$ from the optimal central track position. Targets at declinations from 10.5° to -75.3° , as shown in Figure 2.18 are accessible during windows of opportunity. As the tracker moves along the track the effective collecting area varies and thus SALT has a varying effective diameter of ~ 7 m to 9 m when the tracker is furthest and closest to the optimal central position, respectively.

The tracker is equipped with a 4 mirror spherical aberration corrector (O'Donoghue, 2000), and an atmospheric dispersion compensator (O'Donoghue, 2002), which corrects for the spherical aberration caused by the geometry of the primary mirror and allows access to wavelengths as short as 3200 \AA . These return a corrected flat focal plane with

⁵https://pysalt.salt.ac.za/proposal_calls/2013-2/



Figure 2.18: The visibility annulus of objects observable by SALT. Figure adapted from the SALT call for proposals (2013)⁶

an 8' diameter field of view at prime focus on to the science instruments, with a 1' annulus around it used by the Tracker in a closed-loop guidance system.

2.4.3 SALT Instrumentation

SALT is equipped with the SALT Imaging Camera (SALTICAM) and the RSS science instruments onboard the tracker, and the High Resolution Spectrograph (HRS) and Near Infra-Red Washburn Labs Spectrograph (NIRWALS) science instruments which are fibre-fed from the tracker to their own climate controlled rooms. The RSS is currently the most used instrument on SALT and the only instrument used for spectropolarimetry.

NIRWALS

The NIRWALS is currently being commissioned and will have a wavelength coverage of 8000 to 17000 Å, providing medium resolution spectroscopy at $R = 2000$ to 5000 over Near Infra-Red (NIR) wavelengths (Brink et al., 2022; Wolf et al., 2022). This is ideally suited for studies of nearby galaxies.

⁶https://pysalt.salt.ac.za/proposal_calls/current/ProposalCall.html



Figure 2.19: The optical path of the SALT RSS. Figure adapted from the SALT call for proposals (2023)⁷

HRS

The HRS echelle spectrograph was designed for high resolution spectroscopy at $R = 37000 - 67000$ covering a wavelength range of $3700 - 8900 \text{ \AA}$ and consists of a dichroic beam splitter and two VPH gratings (Nordsieck et al., 2003). This instrument is capable of stellar atmospheric and radial velocity analysis.

SALTICAM

The SALTICAM functions as the acquisition camera and simple science imager with various imaging modes, such as full-mode and slot-mode imaging, and supports low exposure times, down to 50 ms (O'Donoghue et al., 2006). This enables photometry of faint objects, especially at fast exposure times.

RSS

The RSS functions as the primary spectrograph on SALT and can operate in long-slit spectroscopy and spectropolarimetry modes, a narrowband imaging mode, and multi-object and high resolution spectroscopy modes (for an in-depth discussion on operational modes see Kobulnicky et al., 2003, or the latest call for proposals).

The Detector The RSS detector consists of a mosaic of 3 CCD chips with a total pixel scale of $0.1267''$ per unbinned pixel with varying readout times depending on the binning and readout mode. The mosaicking results in a characteristic double ‘gap’ in the frames and resultant spectra taken with the RSS, as seen in Figure 2.16.

The Available Gratings The RSS is equipped with a rotatable magazine of six VPH gratings, as listed in Table 2.1. Observations may be planned using simulator tools pro-

Grating Name	Wavelength Coverage (Å)	Usable Angles (°)	Bandpass per tilt (Å)	Resolving Power (1.25" slit)
PG0300 ⁸	3700 – 9000		3900/4400	250 – 600
PG0700 ⁸	3200 – 9000	3.0 – 7.5	4000 – 3200	400 – 1200
PG0900	3200 – 9000	12 – 20	~ 3000	600 – 2000
PG1300	3900 – 9000	19 – 32	~ 2000	1000 – 3200
PG1800	4500 – 9000	28.5 – 50	1500 – 1000	2000 – 5500
PG2300	3800 – 7000	30.5 – 50	1000 – 800	2200 – 5500
PG3000	3200 – 5400	32 – 50	800 – 600	2200 – 5500

Table 2.1: Gratings available for use with the RSS. Table adapted from the SALT call for proposals (2023).

Linear (°)		Linear-Hi (°)		Circular (°)		Circular-Hi (°)		All Stokes (°)	
$\frac{1}{2}$	$\frac{1}{4}$	$\frac{1}{2}$	$\frac{1}{4}$	$\frac{1}{2}$	$\frac{1}{4}$	$\frac{1}{2}$	$\frac{1}{4}$	$\frac{1}{2}$	$\frac{1}{4}$
0	-	0	-	0	45	0	45	0	0
45	-	45	-	0	-45	0	-45	45	0
22.5	-	22.5	-			22.5	-45	22.5	0
67.5	-	67.5	-			22.5	45	67.5	0
	-	11.25	-			45	45	0	45
	-	56.25	-			45	-45	0	-45
	-	33.75	-			67.5	-45		
		78.75	-			67.5	45		

Table 2.2: Spectropolarimetry waveplate patterns defined for the RSS. The stated angles refer to the angle of the half ($\frac{1}{2}$ -) and quarter ($\frac{1}{4}$ -) waveplate’s optical axis from the perpendicular of the dispersion axis. Table adapted from the SALT call for proposals (2023).

vided by SALT and are performed in the first order only. The RSS has a clear filter, as well as three Ultraviolet (UV) (with differing lower filtering ranges) and one blue order blocking filter available, used in conjunction with the various gratings to block out contamination from the second order.

2.5 RSS Spectropolarimetry

Spectropolarimetry using the RSS is currently commissioned for long-slit linear spectropolarimetry, (I, Q, U) , where observations are taken following the waveplate pattern lists as in Table 2.2. Circular, (I, V) , and all-Stokes, (I, Q, U, V) , spectropolarimetry modes are in commissioning with observations including redundant half-wave plate pairs to be commissioned thereafter.⁹

2.5.1 POLSALT

POLSALT is the current reduction package being constantly developed and used within SAAO/SALT as the official reduction pipeline for spectropolarimetric data taken using

⁸The PG0300 surface relief grating has been replaced with the PG0700 VPH grating as of November 2022 but has been included here as observations using the PG0300 are used in later sections.

⁹Commission status sighted from the latest ‘Polarimetry Observers Guide’ (2024).

SALTs RSS.¹⁰ Newer versions of the software, aptly named the ‘beta version’, include a Graphical User Interface (GUI) as well as limited interactivity during key steps in the reduction process.¹¹ Below we summarize the reduction steps for the “beta version” [23 January 2020] which was adapted in this study.

The steps that make up the reduction pipeline include basic CCD reductions, wavelength calibrations, background subtraction and spectral extraction, raw stokes calculations, final stokes calculations, and visualization of the results. Each step is crucial for good results and thus briefly discussed (a detailed documentation for the reduction steps and purpose may be found at the POLSALT github wiki):

Basic CCD reductions: Basic CCD reductions are run via `imred.py` and apply basic reductions to the raw data necessary before any calibrations may be done. These corrections include overscan subtractions, gain corrections, crosstalk corrections, and mosaicking as well as attaching the bad pixel maps and pixel variance information. Files with basic reductions performed have “mxgbp” prepended to their names. As of February 2022, the reduction step is automatically run for all RSS spectropolarimetric observations as part of the default SALT basic reduction pipeline that is run each day.

Wavelength calibrations: Wavelength calibration and cosmic-ray rejection is performed via `specpolwavemap.py` and separately calibrates the *O*- and *E*-beams, based on the arc frames, and applies a simple cosmic-ray rejection for all science frames. This step is interactive and allows the user to individually fit wavelength calibration maps to each beam. The importance of good correlation between both beams has been touched on previously and will be further discussed in § 3.1. The wavelength calibrated results are saved as an additional extension to each science FITS file, which are prefixed with a “w”, and the *O*- and *E*-beams of the extensions are split into their own sub-extensions.

Spectral extraction: The background subtraction and spectral extraction are run via `specpolextract_dev.py` which corrects for the beam-splitter distortion and tilt, performs sky subtraction, and extracts a one dimensional wavelength dependent spectrum for each beam extension. This step is interactive and, using the brightest trace in the images, allows the user to define regions which span the wavelength axis and which define the background and trace regions for the sky subtraction and spectral extraction. Files with corrections applied are saved with “c” prepended to their names and files which contain the extracted one dimensional spectrum have “e” further prepended to their names.

Raw stokes calculations: Raw stokes calculations are performed via `specpolraw-stokes_dev.py` and identify waveplate pairs for which the intensity, I , and a ‘raw stokes’ signal, S , are calculated as:

¹⁰POLSALT is made freely available via the POLSALT GitHub repository, available at <https://github.com/saltastro/polsalt>. It is strongly advised to follow the wiki for installation instructions.

¹¹Installation files and instructions for the ‘beta version’ utilizing the GUI are available at <http://www.sao.ac.za/~ejk/polsalt/code/> in a TAR GZIP file.

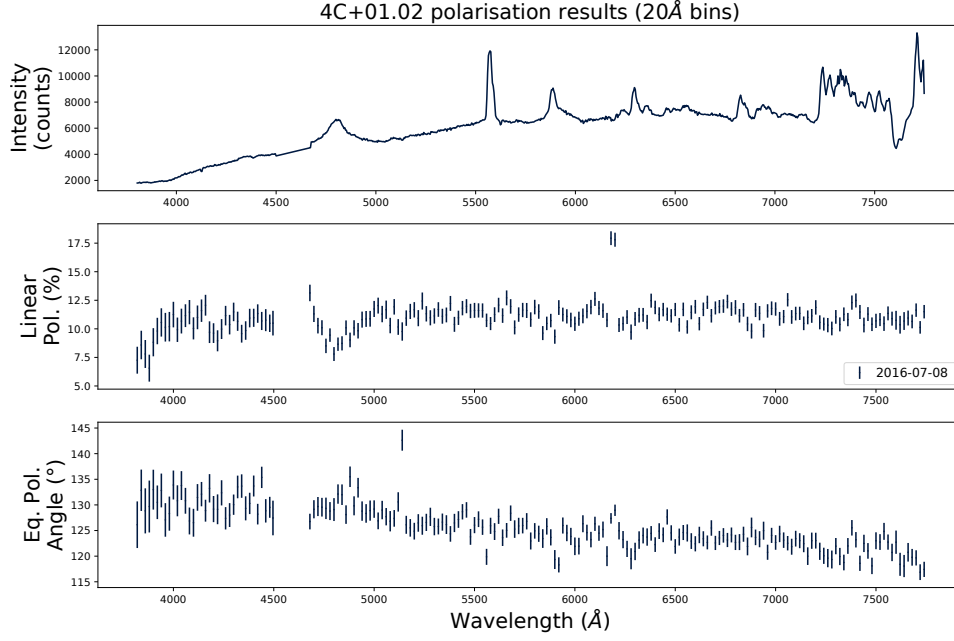


Figure 2.20: A typical plot resulting from the reduction process. Figure adapted from (Cooper et al., 2022)

$$I = \frac{1}{2}(O_1 + O_2 + E_1 + E_2)$$

$$S = \frac{1}{2} \left[\left(\frac{O_1 - O_2}{O_1 + O_2} \right) - \left(\frac{E_1 - E_2}{E_1 + E_2} \right) \right]. \quad (2.47)$$

The raw stokes signal is calculated as the normalized difference of the *O*- and *E*-beams, for a waveplate pair, taken perpendicular to one another. The files generated containing the raw stokes information have a very specific naming style, with most notably the pair of frames used being included.

Final stokes calculations: The Final stokes calculations are performed via **specpol-finalstokes.py** and, using the waveplate pattern along with the raw stokes signals, calibrates for polarimetric zero-point and waveplate efficiency calibrations and calculates the final stokes parameters. Before the final stokes calculations are performed, data culling is applied to the raw stokes to eliminate outlier results which may arise due to, for example, atmospheric conditions. Data culling compares observation cycles against one another, compares the deviation of the means which estimate the systematic polarization baseline fluctuations (due to imperfections in repeatability), and performs a chi-squared analysis to eliminate outliers.

Visualization: Plotting the results of the spectropolarimetric reduction process uses **specpolview.py** and generates a plot of the Intensity, Linear Polarization (%), and Equatorial Polarization Angle (°) against a shared wavelength axis, as seen in Figure 2.20. This step is interactive and various options, such as the wavelength range, binning, etc., are available.

Post-processing analysis: Generally, the plot of the spectropolarimetric results is the stopping point for most reduction procedures as it contains or creates the desired results. However, additional tools exist which may be used after the polarization reductions have been completed, and which are not represented in the GUI, namely, flux calibration and synthetic filtering.

Flux-calibrations are performed via **specpolflux.py** and are only intended for shape corrections of the spectrum. Additionally, the flux database file must exist for the standard observed and must be copied over to the working science directory.

Synthetic filtering is calculated via **specpolfilter.py** and computes the synthetically filtered polarization results. The filters which can be synthesized are the Johnson U , B , and V filter curves from the SALTICAM filters, as well as the Cousins R and I filter curves, along with any user defined wavelength dependent throughput.

Chapter 3

Developed Tools

This chapter contains an overview of why supplementary tools were deemed necessary for an already working reduction process (§ 3.1), which aspects of the reduction process have been altered, replaced, or added (§ 3.2, 3.3), and finally what an updated reduction process consists of using a combination of all software (§ 3.4).

3.1 Limitations of POLSALT and the Need for a Supplementary Tool

The creation of supplementary tools for POLSALT spectropolarimetric reductions stem from, primarily, the limitations of the wavelength calibration process and a need for a way to compare wavelength solutions across matching O and E polarization beams. Due to the time-consuming process of recalibrating the wavelength solutions it is not feasible to perform the wavelength calibrations time and time again for any amount of reductions larger than a handful of observations.

The prime motivation of finding an alternate method of wavelength calibrating the data stemmed from a large backlog of unused data taken using the *PG0300*. The only arc available for the *PG0300* with a close enough articulation and grating angle (~ 10.68 and ~ 5.38 , respectively) was SALT’s Argon lamp which displayed sparse spectral features with large gaps over the wavelength range at these grating and articulation angles. This often lead to inconsistent wavelength solutions, or failed altogether, through POLSALT, since minor deviations of identified spectral features may result in large deviations in regions with no spectral features.

The chosen solution was to use a well established tool to perform the wavelength calibration - one which allows for rapid recalibrations as well as provides a familiar interface with which the user can analyze their wavelength solutions. IRAF provides this familiar environment and reliability, even considering it’s age and limited community development. Unfortunately, IRAF is unable to natively parse the file structure implemented by POLSALT ‘as is’ and formatting of the data structures are necessary for integration purposes. This restructuring works both ways as once the IRAF reductions are complete the format must be reformatted to match that of the POLSALT output such that the reduction process may carry on in POLSALT.

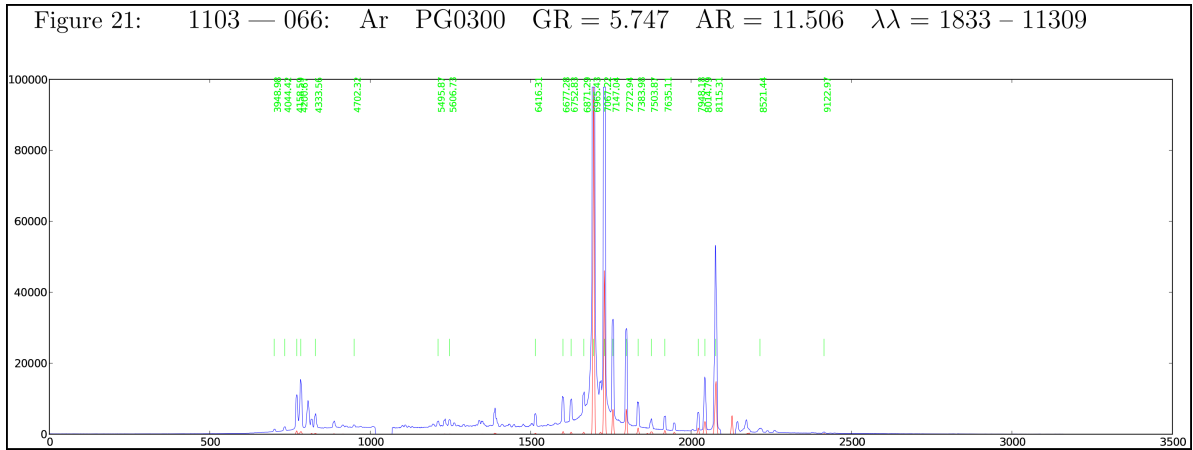


Figure 3.1: One of many Argon arc lamp spectra as provided by SALT for line identification. Plot adapted from SALT’s published Longslit Line Atlases (as of 2024),¹ resized to fit within the document margins but otherwise unchanged.

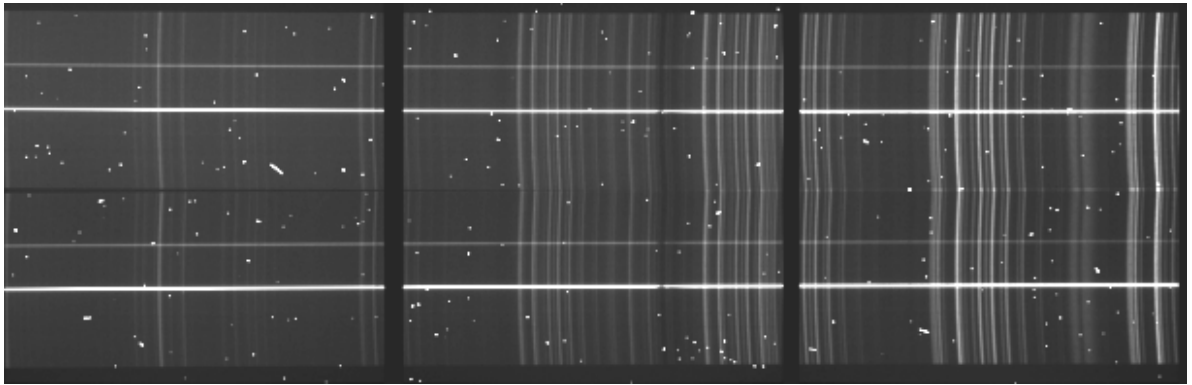


Figure 3.2: The science extension of a typical POLSALT FITS file after basic CCD reductions have been completed.

3.2 Wavelength calibrations - Supplementary Tools and IRAF

The supplementary tools offer an alternate procedure for wavelength calibrations for the POLSALT pipeline. This procedure can be broken into three unique steps: the parsing of POLSALT data into an IRAF friendly format, referred to as splitting; the wavelength calibration performed in IRAF; and the reformatting of the data with its wavelength calibration back into the format expected by POLSALT, referred to as joining.

3.2.1 Splitting the POLSALT pre-calibration files

As mentioned previously, the format of the Flexible Image Transport System (FITS) file created by POLSALT after basic CCD reductions and that expected by IRAF to be used for the wavelength calibrations are incompatible. A typical FITS file created by the POLSALT basic CCD reductions process contains a primary header along with the various image extensions, all of which include the trace for both polarimetry beams, as seen in Figure 3.2. IRAF deals best with a singular trace, and therefore a singular polarization beam, at a time.

¹low resolution’ Ar plot sourced from <https://astronomers.salt.ac.za/data/salt-longslit-line-atlas/>

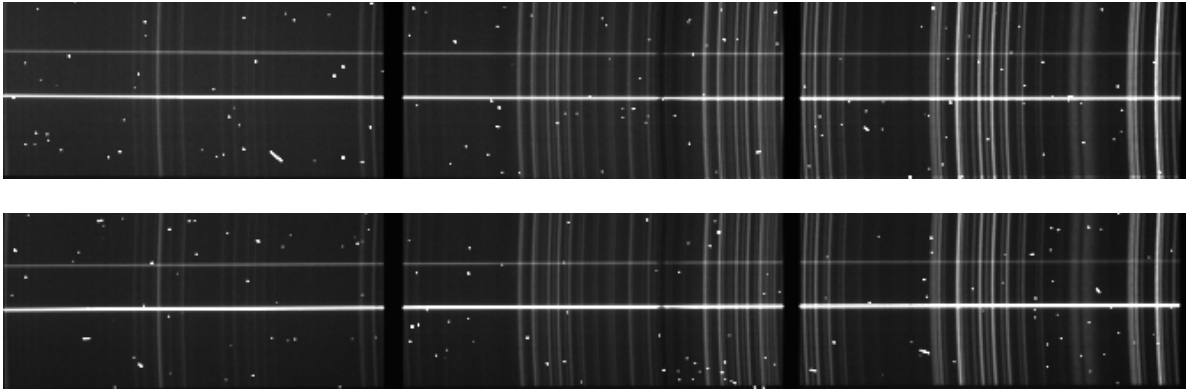


Figure 3.3: The split *O*- and *E*-beams as handed to IRAF.

In an attempt to simplify the IRAF reduction procedure it was decided to split the polarization beams into their own files, as the parameters of IRAF tasks generally handle lists of files better than subregions of the same Header Data Unit (HDU), and generally allowed for easier calibrations further down the IRAF wavelength calibration process.

The POLSALT files with basic CCD reductions applied, namely FITS files with the prefix ‘mxgpb’ (§ 2.5.1), are used as the starting point for the supplementary tool’s `split` method. Running `split` finds all the FITS files for wavelength calibration within the working directory, creates two empty HDU structures for each sub-extension of the FITS file, and appends all science and header data necessary for wavelength calibration to the relevant HDU structure.

As the intent was always to parse the wavelength function back into POLSALT it was decided to keep these temporary FITS files as light as possible. This is especially necessary when considering the amount of frames that must be taken for a single spectropolarimetric observation, and then how the number of observations increases for long term studies.

To aid the IRAF wavelength calibrations, row cropping and file list creation were introduced into the `split` method to ignore the regions without a trace either side of the frame, and to list the *O*- and *E*-beam FITS files, respectively. The row cropping was decided on as IRAF does not handle the empty rows well, specifically when it comes to the `reidentify` task. Otherwise, defaults, such as which row to split the beams along, were kept as close to the POLSALT pipeline as possible.

3.2.2 IRAF wavelength calibration

IRAF is a collection of software designed specifically for the reduction and analysis of astronomical images and spectra. The software consists of many tasks which perform specific operations and which are grouped into relevant packages. Only a brief overview of the tasks will be provided here as every researcher, university, and research group have their own preferred wavelength calibration procedures and often use specific parameters for the various IRAF tasks (e.g. the order and type of the polynomial used in `identify`, etc.).

A useful IRAF task that will not be discussed but nevertheless deserves a mention is

the `mkscript` task in the `system` package which allows a user to create and save a task along with the defined parameters as a file which can later be called as a script. It is instrumental as a scripting aid and is what allows IRAF its rapid recalibrations of the wavelength solutions.

For the alternate wavelength calibrations, the relevant tasks, in order, are `identify` and `reidentify` located in the `noao.onedspec` package, and the `fitcoords` and optionally the `transform` tasks located under the `noao.twodspec.longslit` package. These tasks produce a two-dimensional wavelength solution and thus must all be run twice to create the different wavelength solutions for each of the two spectropolarimetric beams.

Identify The `identify` task is used to interactively determine a one-dimensional wavelength function across a chosen row of an arc exposure by identifying features in the spectrum with known wavelengths. `identify` gives the first approximation of the wavelength solution, which is saved to a local database, and is built on in subsequent tasks. It is thus imperative that the initial fit is done well to minimize errors further down the calibration process.

The process of using `identify` consists of identifying known features spanning the entire wavelength range and then removing identified features which negatively impact the wavelength solution. A balance must be found between the number of identified features and parameters of the fit against the deviation of the fit from the known features.

Reidentify The `reidentify` task is used to run the `identify` task autonomously and repeatedly across the entirety of the arc exposure at a defined interval. `reidentify` uses the one-dimensional wavelength solution stored in the database created by the initial `identify` call and shifts the identified points to match their known spectral features. The task may fail based on a number of defined conditions, most common of which is the loss of features as the task moves further from the row at which the user ran `identify`.

When running `reidentify` non-interactively, it is recommended to set the `verbose` parameter to ‘yes’ as this will allow immediate confirmation whether the task quit early or not. Regardless of where the task ended, the newly defined wavelength solutions are appended to the local database.

Fitcoords The `fitcoords` task is used to combine the collection of one-dimensional wavelength solutions in the local database to a two-dimensional surface function. This surface function is the final two-dimensional wavelength solution and is what is needed to convert the IRAF formatted wavelength calibrated FITS files back into the POLSALT format.

The process of using `fitcoords`, follows closely to that of `identify` and consists of examining the distribution of identified points and eliminating any points that `reidentify` may have misidentified. By eliminating outliers with bad residuals and modifying the two-dimensional surface function type and degree, the overall error of the fit decreases, matching more closely to what the ‘true’ wavelength solution is.

Transform The `transform` task is an optional step in the IRAF wavelength calibration process but is good to perform since it is quick to run and easy to script. `transform` converts the $(pixel, pixel)$ units stored in the exposure to $(wavelength, pixel)$ units which allows for an immediate check of whether the wavelength solution was found correctly. Any error in the wavelength solution will be easily spotted in the transformed images and may range from minor, such as the arc exposure’s arc lines or science exposure’s sky lines not being straight across the columns of the frame, to more severe, such as the wavelength solution completely readjusting the frame to an incoherent mess.

TODO: Include poor and good transformed image examples?

3.2.3 Joining the wavelength calibrated files

As mentioned previously, the format of the FITS file created by IRAF after wavelength calibrations and that expected by POLSALT for the `spectra extraction` are incompatible. A typical FITS file expected by the POLSALT `spectra extraction` contains a primary header along with the various image extensions, the most notable extension being the newly added wavelength extension. All images contained within the extensions have the trace for both polarimetry beams split, as seen in Figure 3.5 and the headers of each extension updated.

All pieces necessary to recreate the POLSALT wavelength calibrated FITS files exist once the IRAF procedure to generate the database entry for the two-dimensional wavelength solution is complete. The `join` method of the supplementary tools is used at this point and, once run, automatically creates the desired files.

Running `join` finds all the relevant FITS and local database files necessary to run the POLSALT `spectra extraction`, creates an empty HDU structure for each pair of matching spectropolarimetric beams, copies over the extensions and their respective image and header information, checks and corrects the trace splitting to best match that of POLSALT, appends a new extension and parses the database wavelength solutions into the POLSALT intensity-wavelength format, cleans the science extension for cosmic rays, and does some house-cleaning to align the finalized FITS files to those created when using the ‘pure’ POLSALT pipeline.

The FITS files created by the `join` method and POLSALT pipeline’s `wavelength calibration` methods are almost identical. The only difference between the FITS files is the shape of the images stored within them, reflected also through specifically the ‘NAXIS2’ header keyword, since `split` introduces a cropping. It was deemed unnecessary to reintroduce the cropped region as it is promptly discarded in the following POLSALT `spectra extraction` process and raises no issues when left out. Otherwise, both the `join` method and POLSALT `wavelength calibration` update the headers to reflect the new shape of the data and data type, through header keywords ‘CTYPE3’ and ‘BITPIX’, respectively.

The wavelength extension is created entirely by `join` by appending a blank extension to the HDU and filling the image pixels with their respective wavelength value. This is done entirely by `join` which parses the wavelength database file and creates a function which provides the corresponding wavelength when provided with a $(pixel, pixel)$ position.

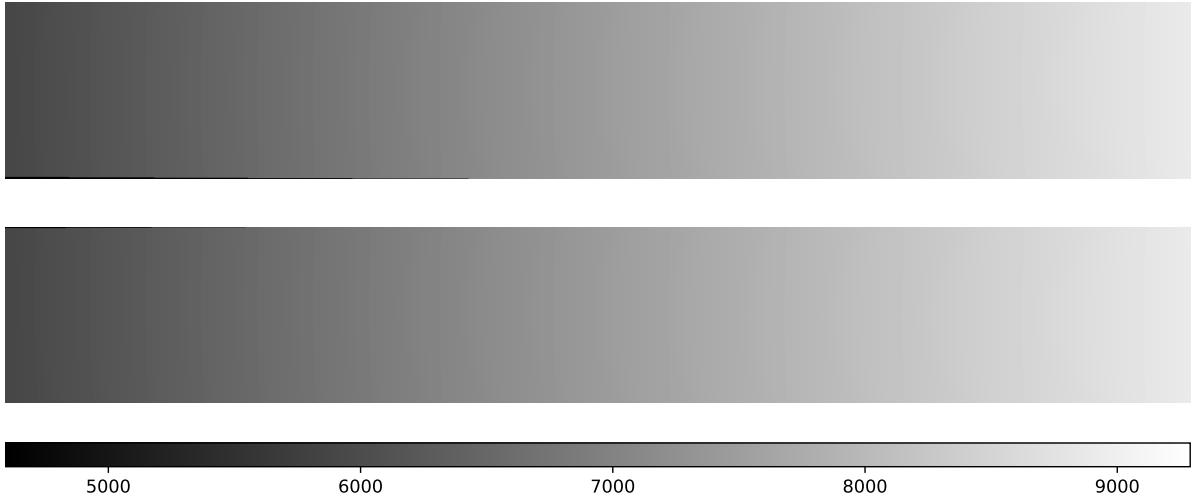


Figure 3.4: The wavelength extension of a FITS file ready to be handed back to the POLSALT pipeline.

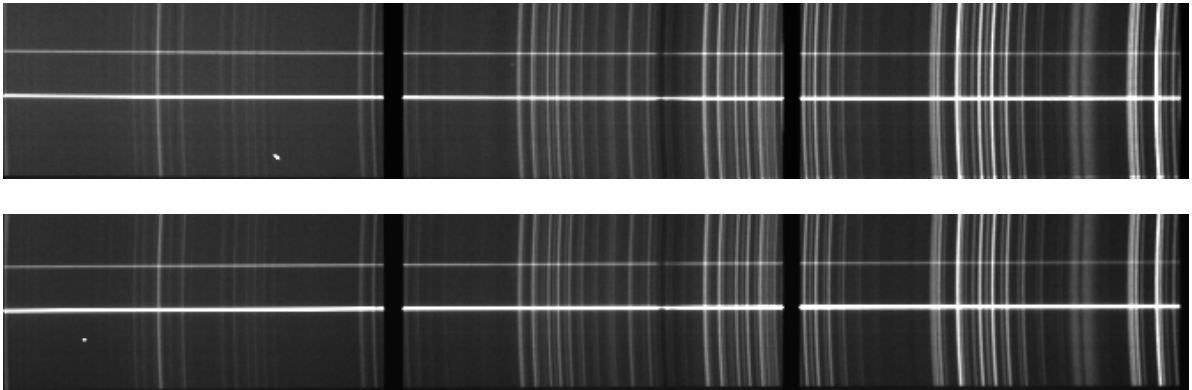


Figure 3.5: The science extension of a FITS file ready to be handed back to the POLSALT pipeline.

This is used to fill the pixels of the wavelength extension with their respective wavelength, as seen in Figure 3.4. Note that regions that fall outside the trace are masked by setting the wavelength extensions corresponding pixel value to 0.

`join` cleans the science extension of cosmic rays using the `lacosmic` python package which was specifically designed for this purpose and uses the L.A. Cosmic algorithm, based on Laplacian edge detection. The parameters used for cosmic ray cleaning were chosen based on the properties of the RSS, specifically the read noise and gain, as well as a publication and suggestions by the algorithm’s creator (van Dokkum, 2001). The chosen parameters work well for all but the worst of cosmic rays, as can be seen when comparing Figures 3.3 and 3.5.

The wavelength extension is masked to remove any impossible wavelengths and also corrected for the skewing of the trace introduced by the wollaston element. The skewing must be added to the wavelength extension since POLSALT introduces a wollaston correction in the `spectra extraction` process. Finally, the Bad Pixel Map (BPM) extension is masked to reflect the valid wavelength calibrated regions for both spectropolarimetric beams and the files are saved with the POLSALT wavelength calibrated ‘`wmxgbp`’ prefix.

3.3 Additional Tools

Before creating the supplementary tool's `split` and `join` methods used to perform wavelength calibrations in IRAF, it was deemed necessary to create a tool to allow for the comparison of the wavelength solutions between the extracted spectra of the *O* and *E* beams, referred to as `correlate`. The scope was later expanded to allow for the inspection of the cross-row and cross-column axes of the wavelength solutions as the IRAF wavelength calibration procedure provided much more flexibility.

3.3.1 Sky line comparisons

TODO: Include example of skyline result

Sky line comparisons serve two unique yet interconnected services. Firstly, they naively transform the wavelength calibrated frames, without conserving flux, allowing the user confirmation of the variation of sky lines across the columns of the frame, and secondly, they compare the wavelength position of the sky lines with the SALT sky lines,² allowing confirmation of the wavelength solution at positions across the rows of the frame. The file used for skyline comparisons may be the IRAF `transform` FITS file, which allows for flux conservation through the 'flux' parameter.

The `skyline` method loads the wavelength calibrated files, transforms the frames (as described above) if the frame was not transformed by IRAF's `transform` method, divides out the continua, compares the cross-column sky lines to those of a single row, and compares the wavelength position of said sky lines to a list of sky lines known by SALT.

Determining if there is an inaccuracy in the wavelength solution in the spatial (*y*, or vertical) axis is relatively straightforward as a perfect wavelength solution will remove any horizontal variation of the sky lines. Any horizontal deviation of the sky lines after transformation reflects a poor fit of the wavelength solution. Any vertical variation may be found through a quick visual inspection of a transformed frame, as mentioned previously, but may be inspected more thoroughly using the `skyline` method. As mentioned, the sky lines are averaged and compared to sky lines of a typical row. A wavelength solution exhibiting a poor fit across the spatial axis will display broader averaged sky lines than that of a relatively good fit.

As no features, other than the trace of sources exposed across a frame, exist that uniformly cover the wavelength (*x*, horizontal) axis of a typical frame, determining if the horizontal fit of the wavelength solution is more challenging. Thankfully, SALT has published a sky line atlas which we may make use of. By first considering the spatial fit of the wavelength solution, it is ensured that the wavelength positions of all sky lines are well-defined. Comparisons may now be made to the wavelength positions measured by SALT. Minor variations in the comparison of the sky lines are expected, but any uniform trends indicate an underlying poor fit across the wavelength axis of the wavelength solution. A poor horizontal fit is difficult to spot without supplementary tools and may have drastic adverse effect on the final polarization results.

²The first iteration of a sky line atlas is available at <https://astronomers.salt.ac.za/data/salt-longslit-line-atlas/>

3.3.2 Cross correlation

TODO: Include example of correlate result

The `skyline` method allows for confirmation of a single wavelength solution, but has no means for comparing how the wavelength solutions of two polarization beams differ from one another. The difficulty arises in comparing the two spectra since variations between the two are expected and are what define the stokes, and thus final polarization, results. The `correlate` method was created for this express purpose.

The `correlate` method loads the provided FITS files created by the POLSALT `spectra extraction`, removes the continuum and separates the CCD regions. The relevant, separated, CCD regions are then cross correlated and any offset between the spectra may be plotted.

As the stokes results, and thus final polarization results, are determined and are heavily influenced by the differences in the spectra of the different *O* and *E* beams, a direct comparison is not appropriate. Any observed unpolarized light, however, will reflect equally in both polarization beams and so the general trend of the two spectra may reasonably be expected to follow one another. Cross correlation of the two spectra for the different, *O* and *E*, polarization beams allows for a comparison of the features within the spectra as a function of the wavelength displacement.

Sources under spectropolarimetric observation are often expected to vary over time and as such as the ratio of polarized to unpolarized light varies. The accuracy of correlation may decrease as features with differences in the polarized component of the polarization beams change. The differences in the features of the different spectra are often negligible when compared to the overall trend of the spectra and are generally only reflected in a change in the intensity of said features.

Cross correlation is useful when dealing with spectropolarimetric spectra as it allows a comparison of how well aligned the notable features of the spectra are wavelength-wise. Minor deviations between spectra weight the cross correlation less than the more prominent features, and therefore, cross correlation results acquired when using the `correlate` method more accurately reflect any general offset between polarization beams that may not necessarily be found when using the `skyline` method.

3.4 General Reduction Procedure

This section aims to give an overview of the reduction procedure from start to finish and to cover all commands needed to achieve a finalized result. As users all employ a variety of operating systems, language environments, and software setups, not much emphasis will be placed on how to get the software running or the managing of files, only the commands necessary to complete each step of the reduction process, assuming that the software is running as intended.

It is recommended that POLSALT is used through the GUI as it provides a user-friendly environment while also sequentially listing each step of the reduction process

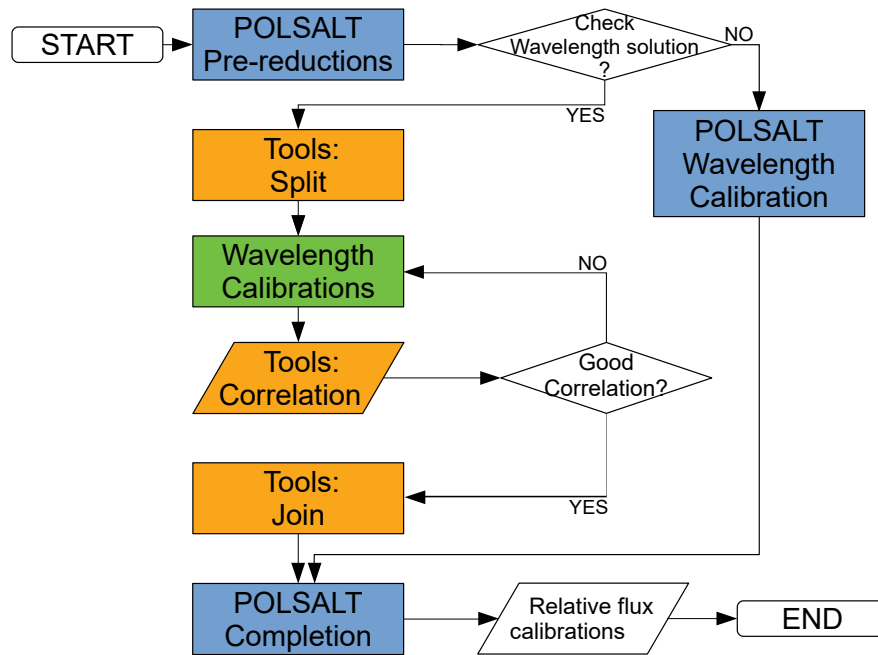


Figure 3.6: A general workflow for data reductions using a combination of POLSALT, IRAF, and the developed supplementary tools.

in a dropdown menu. Reductions are possible, however, purely using a Command Line Interface (CLI) and the POLSALT scripts. It is assumed that usage of POLSALT through the GUI or CLI use the ‘beta’ or ‘basic’ versions, respectively, and that the beta version is launched from the POLSALT directory while the basic version is run by copying over the ‘scripts’ folder to the working directory. The IRAF terminal, once launched, and the CLI supplementary tools are also assumed to be run from the ‘working’ directory. This ensures that commands containing `<.../>` notate the need for the inclusion of relative paths to the desired file or folder.

Help documentation, primarily describing the possible arguments, is available in the CLI for POLSALT and the supplementary tools using the `-h|--help` flag with their respective invocation, such as:

```
> python <.../>Masters --help
```

and for IRAF through the `?|:.help` ‘cursor mode’ options while running an interactive task.

3.4.1 POLSALT Pre-reductions

TODO: Include screenshot of GUI, reference in paragraph

POLSALT requires a file structure such that the raw data received from SALT is located in a folder labeled using the observing date as well as being in a sub-folder labeled raw, such as `YYYYMMDD/raw/`. This directory structure allows POLSALT to create a ‘working’ directory named `YYYYMMDD/sci/` which contains all the files modified during the reduction

process. This allows for separation of reductions of the same data by simply renaming the `sci/` directory.

To launch the GUI, navigate to the POLSALT directory within a CLI and run:

```
> python -W ignore reducepoldataGUI.py &
```

Once the window has launched, ensure that the first and second paths at the top of the window point to the POLSALT and data observation date directories, respectively. The ‘raw image reduction’ may then be selected from the dropdown and run. The POLSALT CLI command:

```
> python scripts/reducepoldata.py <.../>YYYYMMDD
```

then runs the raw image reduction process. It should be noted that the POLSALT CLI command will, by default, attempt to run the wavelength calibration process. This behavior may be stopped by using the `-w` flag when running the command.

3.4.2 Wavelength Calibration

The wavelength calibrations may now be completed in IRAF. This section concerns the procedure for parsing the FITS files to be read by IRAF and POLSALT as well as the relevant task names and methods to be run to complete the calibrations. A base working case of each of the tasks and methods are presented below, but it should be noted that the art of wavelength calibration consists of modifying the parameters to achieve a good calibration function. This process depends heavily and varies greatly based on the user and as such not all use cases can be discussed herein.

Preparing data for IRAF

Splitting the data in the working `sci/` directory may then be done through a CLI using:

```
> python <.../>Masters split
```

The method takes multiple parameters, but default parameters are used where ever possible. The most notable parameters are the directory, which defaults to the current working directory of the CLI, the split row, which defaults to POLSALT’s default center row, and the save prefix, which defaults to ‘`obeam`’ and ‘`ebeam`’. As an aside, the save prefix may be worth changing as, later in the reduction process, the POLSALT raw stokes reductions indiscriminately selects files named `YYYYMMDD/sci/e*.fits`.

IRAF wavelength calibrations

Moving on to IRAF, the wavelength calibrations are performed using the tasks described in § 3.2.2, namely `identify`, `reidentify`, and `fitcoords`, and may be run directly in the IRAF terminal using:³

³Please see the IRAF help docs, available at https://astro.uni-bonn.de/~sysstw/lfa_html/iraf/iraf.html, on the relevant tasks for a comprehensive discussion of the parameters available.

```
cl> identify images
cl> reidentify reference images
cl> fitcoords images fitname
```

where ‘images’ refer to a list or file containing the FITS files relevant to the task, ‘reference’ refers to the FITS file previously identified, and ‘fitname’ refers to the name to be used for the final two-dimensional wavelength solution. The interactive tasks take up the bulk of the reduction time as this is where the fine-tuning of the reduction is done, through the use of cursor commands (otherwise known as colon commands), which allow modification of the parameters mid-reduction. Task parameters may, however, be edited beforehand within the IRAF terminal using the `eparam` task, and optionally saved, and quit or run using a combination of `:w`, and `:q` or `:go` cursor commands, respectively.

It is recommended to create an IRAF Command Language (cl) script for each task to keep track of which parameters were used and for simple recalibrations. The scripts are created using:

```
cl> mkscript script_name.cl
```

which will interactively ask for the task and parameters to be used. Multiple tasks may be appended to an IRAF script, allowing for the parameters of both beams to be tracked. Running an IRAF script may be done by running:

```
cl> cl < script_name.cl
```

but is not suggested for interactive scripts, which run best when simply copied from the `<.../>sci/script_name.cl` file to the IRAF terminal.

Preparing data for POLSALT

The results of the wavelength calibrations may now be parsed back into the format expected by POLSALT. Joining the separate beams with their respective wavelength solutions is once again performed in the CLI and is completed using:

```
> python <.../>Masters join
```

Similar to the `split` procedure mentioned before, the `join` procedure has the same defaults defined and so it is up to a user to keep track of which defaults they decided to change and keep them consistent between the two tasks.

Supplementary checks of the wavelength solution

The supplementary tools and the optional IRAF `transform` task are used as methods for confirming the wavelength solutions across the frame, against reference wavelength positions, and across the polarization beams. They are all discussed here as this section pertains to the supplementary tools and IRAF procedures, but might only be used later on in the reduction process.

The IRAF `transform` task may be run before closing the IRAF environment using:

```
cl> transform images output fitnames
```

where ‘images’ refers to the same pseudonym as used in the previous IRAF task usage examples, ‘output’ refers to the new file name for the transformed input images, and ‘fit-names’ refers to the two-dimensional wavelength function name created by the `fitcoords` task.

The `skyline` method is run in the CLI using:

```
> python <.../>Masters skyline cal_images
```

where ‘cal.images’ refers to either the transformed images, prefixed ‘t’, produced by the IRAF `transform` task or the raw wavelength calibrated frames. The difference in the flux conservation when `skyline` transforms the frames is discussed in § 3.3.1. Otherwise, as with all the other supplementary tools, default parameters also describe the overplotting of the *O*- and *E*-beams, the overplotting of the skylines provided by SALT, and the cross row variation of a frame.

The `correlate` method is run in the CLI using:

```
> python <.../>Masters correlate spec_images
```

where ‘spec.images’ refers to spectra extracted FITS files. If the user wishes to compare the *O*- and *E*-beams of a single file then only that image name is to be provided, otherwise it is assumed that the user wishes to compare the same polarization beam across the files provided. It is worth pointing out here that as the input images are only created after performing the POLSALT `spectra extraction` and thus should only be completed thereafter.

A final reminder is made here about the clash of default naming schemes and wildcard file collection performed by POLSALT. A simple wildcard `mv` move or `rm` remove command may be run in the CLI to deal with the created split files used by IRAF. The remove command may be run using:

```
> rm obeam* ebeam*
```

while moving the files to a new subfolder the may be done using:

```
> mkdir ./split_files/
> mv obeam* ebeam* ./split_files/
```

3.4.3 POLSALT Reduction Completion

Reductions may now be completed using POLSALT. The reduction process consists of correcting for the wollaston tilt, extracting the spectra, creating the stokes files, and displaying the results. As always, the reductions are handled slightly differently for the differing versions.

POLSALT, the basic version

Covering the basic version first, the wavelength solution needs to be applied to all the FITS files and the tilt introduced by the wollaston prism must be corrected for. This is done through the command:

```
> python scripts/correct_files.py w*fits
```

where the 'w*fits' is a wildcard expression that lists the FITS files that have a wavelength extension and returns it to the POLSALT script.

Next, the spectra in each FITS file are extracted using the command:

```
> python scripts/pol_extract.py c*fits --yo A --ye B --dy C
```

where the center row of the spectra for the *O*- and *E*-beams, A and B, as well as the spectral width, C, are integer values and must be provided. These may be found through FITS viewing software such as ds9⁴ or more manually through python.

The Stokes files may then be calculated and created using the command:

```
> python scripts/pol_stokes.py
```

which automatically detects the FITS files using the wildcards 'e*fits' for raw stokes and '*_h*fits' for the final stokes calculations. The deletion of the FITS files created in the supplementary `split` method may be deleted in the `join` method specifically to avoid this naming convention clash, but may also be avoided by providing an alternate default subscript to the supplementary methods.

Finally, the results of the stokes calculations may be viewed using the command:

```
> python polsalt/specpolview.py *_stokes.fits
```

where a file name, which may also use a wildcard, is provided as well as optional parameters to define the binning (`bin=[int]A` where [int] refers to an actual integer value), error bars (`errors=True|False`), choice of plot (`type=Ipt|Iqu` for unbinned intensity and either polarization percentage and polarization angle, or *Q* and *U* stokes parameters), save options (`save=[text][plot]` where either or both 'text' and 'plot' may be provided), and a debug mode (`debug=False|True`).

POLSALT, the beta version

The POLSALT beta version has access to a GUI but may also be run as a script. The script will be discussed before the GUI as it is straightforward to run and modify.

Firstly, to run the POLSALT beta script, it is suggested to copy over the `reducepol-data_sc.py` to the working directory. In general, running the script as:

```
> python reducepoldata_sc.py YYYYMMDD
```

⁴Available at <https://sites.google.com/cfa.harvard.edu/saoimageds9>

will run the entire reduction process interactively without the need to select which process to run next. For the purposes of using the script alongside IRAF wavelength calibrations, a few changes must be made. The script may either be run with a break inserted before the call to the wavelength calibration, `specpolwavmap`, and later rerun with all processes before spectral extraction, `specpolextract_sc`, commented out, or may be split into two separate files which cover the pre- and post- wavelength calibration steps and run when appropriate.

The POLSALT beta `reducepoldata_sc.py` copies a `script.py` file into the science working directory, ‘YYYYMMDD/sci/’, which provides analysis scripts for analysis and modification of the POLSALT beta results. These tools consist of data culling for the final stokes calculations, text and plot output (the same as the basic version of POLSALT’s `specpolview.py`), relative flux calibration corrections, and synthetic filtering of polarization results. The POLSALT analysis scripts may be run using:

```
> python script.py
```

followed by `specpolfinalstokes.py`, `specpolview.py`, `specpolflux.py`, or `specpolfilter.py`, respectively, for the analysis modes mentioned previously. Each mode has its own usage parameters, and it is suggested that a user look up the documentation before attempting to use any of them.⁵

Finally, the reduction process using the POLSALT GUI is completed by selecting and, when applicable, interactively modifying the reduction step through the interactive windows, one-by-one, from the GUIs dropdown menu.

The reduction process when using the POLSALT beta version is straightforward and is made even more so by the inclusion of the GUI. As no commands are necessary, save for those to launch the GUI window, not much can be said of the reduction process. Excellent resources, created by the SALT (**TODO: SAAO?**) team, are available online for any queries about the reduction process using any version of POLSALT, including the GUI.⁶

⁵A description of the use of each analysis script is available from <https://github.com/saltastro/polsalt/wiki/Linear-Polarization-Reduction.--Beta-version> and is exhaustive enough for general use, but the source code is also made available and should be consulted before usage.

⁶See the official POLSALT wiki or alternative online resources such as SALT workshop slides.

Chapter 4

Testing

TODO: Add all tests done and comparisons.

- 3C 279
- 4C+01.02
- David data (not in next section publications because still during pipeline development. Reductions done through polsalt, but after publication used as preliminary testing data)

Chapter 5

Science Applications

TODO: short introduction to chapter contents

5.1 Application to Spectropolarimetric Standards

TODO: Spectropolarimetric standards (4 highly polarised, 2 non-polarised)

- Background on objects
- Reductions
- Actual results - comparison of polsalt results to supplementary pipeline results
- Science results, what the results can tell us and why it is useful, also comparison of results to FORS1/2 published data, focus on the polarisation results

5.2 Application in publications

TODO: Summary of results from papers in appendix.

- Hester paper(s)
- Joleen proceedings and work
- My proceedings

TODO: 3C 279 and 4C+01.02

- Give Background on objects, Reduction steps, and Science results (what the results can tell us and why it is useful)
- (comparison of polsalt results to supplementary pipeline results will be in testing)

Chapter 6

Conclusions

TODO: A summary of the dissertation, main focus on the results and that the supplementary pipeline is a success since it allows an alternate method using IRAF to wavelength calibrate the polysalt data.

Acknowledgements

I hereby acknowledge and express my sincere gratitude to the following parties for their valuable contributions:

- **TODO: Add acknowledgements!**

List of Acronyms

ADC	Analog-to-Digital Converter
BPM	Bad Pixel Map
CCD	Charged-Coupled Device
CLI	Command Line Interface
CMOS	Complementary Metal-Oxide-Semiconductor
FITS	Flexible Image Transport System
FWHM	Full Width at Half Maximum
GUI	Graphical User Interface
HDU	Header Data Unit
HET	Hobby-Eberly Telescope
HRS	High Resolution Spectrograph
L+45°	Linear +45° Polarized
L−45°	Linear −45° Polarized
LCP	Left Circularly Polarized
LHP	Linear Horizontally Polarized
LVP	Linear Vertically Polarized
NIR	Near Infra-Red
NIRWALS	Near Infra-Red WASHburn Labs Spectrograph
RCP	Right Circularly Polarized
RSS	Robert Stobie Spectrograph
S/N	Signal-to-Noise Ratio
SAAO	South African Astronomical Observatory
SALT	Southern African Large Telescope
SALTICAM	SALT Imaging Camera
UV	Ultraviolet
VPH	Volume Phase Holographic

Bibliography

R. R. J. Antonucci and J. S. Miller. Spectropolarimetry and the nature of NGC 1068. ApJ, 297:621–632, October 1985. doi: 10.1086/163559.

George B. Arfken and Hans J. Weber. Mathematical methods for physicists, 1999.

S. Bagnulo, M. Landolfi, J. D. Landstreet, E. Landi Degl’Innocenti, L. Fossati, and M. Sterzik. Stellar spectropolarimetry with retarder waveplate and beam splitter devices. Publications of the Astronomical Society of the Pacific, 121(883):993, aug 2009. doi: 10.1086/605654. URL <https://dx.doi.org/10.1086/605654>.

Erasmus Bartholinus. Experimenta crystalli islandici dis-diaclastici, quibus mira et insolita refractio detegitur (copenhagen, 1670). Edinburgh Philosophical Journal, 1:271, 1670.

D. Scott Birney, Guillermo Gonzalez, and David Oesper. Observational Astronomy - 2nd Edition. Cambridge University Press, 2006. doi: 10.2277/0521853702.

Janus D. Brink, Moses K. Mogotsi, Melanie Saayman, Nicolaas M. Van der Merwe, Jonathan Love, and Alrin Christians. Preparing the SALT for near-infrared observations. In Heather K. Marshall, Jason Spyromilio, and Tomonori Usuda, editors, Ground-based and Airborne Telescopes IX, volume 12182 of Society of Photo-Optical Instrumentation Engineers (SPIE) Conference Series, page 121822E, August 2022. doi: 10.1117/12.2627328.

David A. H. Buckley, Gerhard P. Swart, and Jacobus G. Meiring. Completion and commissioning of the Southern African Large Telescope. In Larry M. Stepp, editor, Society of Photo-Optical Instrumentation Engineers (SPIE) Conference Series, volume 6267 of Society of Photo-Optical Instrumentation Engineers (SPIE) Conference Series, page 62670Z, June 2006. doi: 10.1117/12.673750.

Christian Buil. CCD astronomy : construction and use of an astronomical CCD camera / Christian Buil ; translated and adapted from the French by Emmanuel and Barbara Davoust. Willmann-Bell, Richmond, Va, 1st english ed. edition, 1991. ISBN 0943396298.

Eric B. Burgh, Kenneth H. Nordsieck, Henry A. Kobulnicky, Ted B. Williams, Daragh O’Donoghue, Michael P. Smith, and Jeffrey W. Percival. Prime Focus Imaging Spectrograph for the Southern African Large Telescope: optical design. In Masanori Iye and Alan F. M. Moorwood, editors, Instrument Design and Performance for Optical/Infrared Ground-based Telescopes, volume 4841 of Society of Photo-Optical

- Instrumentation Engineers (SPIE) Conference Series, pages 1463–1471, March 2003. doi: 10.1117/12.460312.
- Subrahmanyan Chandrasekhar. Radiative transfer, 1950.
- Marshall H. Cohen. Genesis of the 1000-foot Arecibo dish. Journal of Astronomical History and Heritage, 12(2):141–152, July 2009.
- E. Collett. Field Guide to Polarization. Field Guides. SPIE Press, 2005. ISBN 9780819458681. URL <https://books.google.co.za/books?id=5lJwcCsLbLsC>.
- J. Cooper, B. van Soelen, and R. Britto. Development of tools for SALT/RSS spectropolarimetry reductions: application to the blazar 3C279. In High Energy Astrophysics in Southern Africa 2021, page 56, May 2022. doi: 10.22323/1.401.0056.
- G. Dahlquist and Å. Björck. Numerical Methods. Dover Books on Mathematics. Dover Publications, 2003. ISBN 9780486428079. URL <https://books.google.co.ls/books?id=armfeHpJIwAC>.
- E. Landi Degl’Innocenti, S. Bagnulo, and L. Fossati. Polarimetric standardization, 2006.
- Egidio Landi Degl’Innocenti. The physics of polarization. Proceedings of the International Astronomical Union, 10(S305):1–1, 2014.
- Egidio Landi Degl’Innocenti and M. Landolfi. Polarization in Spectral Lines, volume 307. Springer Dordrecht, 2004. doi: 10.1007/978-1-4020-2415-3.
- Königlich Bayerische Akademie der Wissenschaften. Denkschriften der Königlichen Akademie der Wissenschaften zu München für das Jahre 1820 und 1821, volume 8. Die Akademie, 1824. URL <https://books.google.co.za/books?id=k-EAAAAAYAAJ>.
- J. F. Donati, M. Semel, B. D. Carter, D. E. Rees, and A. Collier Cameron. Spectropolarimetric observations of active stars. MNRAS, 291(4):658–682, November 1997. doi: 10.1093/mnras/291.4.658.
- I. V. Florinsky and A. N. Pankratov. Digital terrain modeling with the chebyshev polynomials. Machine Learning and Data Analysis, 1(12):1647 – 1659, 2015. doi: 10.48550/ARXIV.1507.03960. URL <https://arxiv.org/abs/1507.03960>.
- Augustin Fresnel. Oeuvres completes d’Augustin Fresnel: 3. Imprimerie impériale, 1870.
- L. M. Freyhammer, M. I. Andersen, T. Arentoft, C. Sterken, and P. Nørregaard. On Cross-talk Correction of Images from Multiple-port CCDs. Experimental Astronomy, 12(3):147–162, January 2001. doi: 10.1023/A:1021820418263.
- David J Griffiths. Introduction to electrodynamics, 2005.
- George E. Hale. The Zeeman Effect in the Sun. PASP, 20(123):287, December 1908. doi: 10.1086/121847.
- George E. Hale. 16. On the Probable Existence of a Magnetic Field in Sun-Spots, pages 96–105. Harvard University Press, Cambridge, MA and London, England, 1979. ISBN 9780674366688. doi: doi:10.4159/harvard.9780674366688.c19. URL <https://doi.org/10.4159/harvard.9780674366688.c19>.

- P. D. Hale and G. W. Day. Stability of birefringent linear retarders(waveplates). Appl. Opt., 27(24):5146–5153, Dec 1988. doi: 10.1364/AO.27.005146. URL <https://opg.optica.org/ao/abstract.cfm?URI=ao-27-24-5146>.
- E. Hecht. Optics. Pearson Education, Incorporated, 2017. ISBN 9780133977226. URL <https://books.google.co.za/books?id=ZarLoQEACAAJ>.
- Steve B. Howell. Handbook of CCD Astronomy, volume 5. Cambridge University Press, 2006.
- Christian Huygens. Treatise on light, 1690. translated by Thompson, s. p., 1690. URL <https://www.gutenberg.org/files/14725/14725-h/14725-h.htm>.
- Mourad E. H. Ismail. Classical and Quantum Orthogonal Polynomials in One Variable. Encyclopedia of Mathematics and its Applications. Cambridge University Press, 2005. doi: 10.1017/CBO9781107325982.
- James Janesick, James T. Andrews, and Tom Elliott. Fundamental performance differences between CMOS and CCD imagers: Part 1. In David A. Dorn and Andrew D. Holland, editors, Society of Photo-Optical Instrumentation Engineers (SPIE) Conference Series, volume 6276 of Society of Photo-Optical Instrumentation Engineers (SPIE) Conference Series, page 62760M, June 2006. doi: 10.1117/12.678867.
- F.A. Jenkins and H.E. White. Fundamentals of Optics. International student edition. McGraw-Hill, 1976. ISBN 9780070323308. URL <https://books.google.co.za/books?id=dCdRAAAAMAAJ>.
- Christoph U. Keller. Instrumentation for astrophysical spectropolarimetry. Astrophysical Spectropolarimetry, 1:303–354, 2002.
- G. Kirchhoff and R. Bunsen. Chemische Analyse durch Spectralbeobachtungen. Annalen der Physik, 189(7):337–381, January 1861. doi: 10.1002/andp.18611890702.
- Henry A. Kobulnicky, Kenneth H. Nordsieck, Eric B. Burgh, Michael P. Smith, Jeffrey W. Percival, Ted B. Williams, and Darragh O’Donoghue. Prime focus imaging spectrograph for the Southern African large telescope: operational modes. In Masanori Iye and Alan F. M. Moorwood, editors, Instrument Design and Performance for Optical/Infrared Ground-based Telescopes, volume 4841 of Society of Photo-Optical Instrumentation Engineers (SPIE) Conference Series, pages 1634–1644, March 2003. doi: 10.1117/12.460315.
- Gerard Leng. Compression of aircraft aerodynamic database using multivariable chebyshev polynomials. Advances in Engineering Software, 28(2):133–141, 1997. ISSN 0965-9978. doi: [https://doi.org/10.1016/S0965-9978\(96\)00043-9](https://doi.org/10.1016/S0965-9978(96)00043-9). URL <https://www.sciencedirect.com/science/article/pii/S0965997896000439>.
- Dave Litwiller. Ccd vs. cmos. Photonics spectra, 35(1):154–158, 2001.
- Dongyue Liu and Bryan M. Hennelly. Improved wavelength calibration by modeling the spectrometer. Applied Spectroscopy, 76(11):1283–1299, 2022. doi: 10.1177/00037028221111796. URL <https://doi.org/10.1177/00037028221111796>. PMID: 35726593.

- Etienne L. Malus. Sur une propriété de la lumière réfléchie. Mém. Phys. Chim. Soc. d’Arcueil, 2:143–158, 1809.
- I. Newton and W. Innys. Opticks:: Or, A Treatise of the Reflections, Refractions, Inflections and Colours of Light. Opticks:: Or, A Treatise of the Reflections, Refractions, Inflections and Colours of Light. William Innys at the West-End of St. Paul’s., 1730. URL <https://books.google.co.za/books?id=GnAFAAAAQAAJ>.
- Kenneth H. Nordsieck, Kurt P. Jaehnig, Eric B. Burgh, Henry A. Kobulnicky, Jeffrey W. Percival, and Michael P. Smith. Instrumentation for high-resolution spectropolarimetry in the visible and far-ultraviolet. In Silvano Fineschi, editor, Polarimetry in Astronomy, volume 4843 of Society of Photo-Optical Instrumentation Engineers (SPIE) Conference Series, pages 170–179, February 2003. doi: 10.1117/12.459288.
- D. O’Donoghue, D. A. H. Buckley, L. A. Balona, D. Bester, L. Botha, J. Brink, D. B. Carter, P. A. Charles, A. Christians, F. Ebrahim, R. Emmerich, W. Esterhuyse, G. P. Evans, C. Fourie, P. Fourie, H. Gajjar, M. Gordon, C. Gumede, M. de Kock, A. Koeslag, W. P. Koorts, H. Kriel, F. Marang, J. G. Meiring, J. W. Menzies, P. Menzies, D. Metcalfe, B. Meyer, L. Nel, J. O’Connor, F. Osman, C. Du Plessis, H. Rall, A. Riddick, E. Romero-Colmenero, S. B. Potter, C. Sass, H. Schalekamp, N. Sessions, S. Siyengo, V. Sopela, H. Steyn, J. Stoffels, J. Scholtz, G. Swart, A. Swat, J. Swiegers, T. Tiheli, P. Vaisanen, W. Whittaker, and F. van Wyk. First science with the Southern African Large Telescope: peering at the accreting polar caps of the eclipsing polar SDSS J015543.40+002807.2. MNRAS, 372(1):151–162, October 2006. doi: 10.1111/j.1365-2966.2006.10834.x.
- Darragh O’Donoghue. Correction of spherical aberration in the Southern African Large Telescope (SALT). In Philippe Dierickx, editor, Optical Design, Materials, Fabrication, and Maintenance, volume 4003 of Society of Photo-Optical Instrumentation Engineers (SPIE) Conference Series, pages 363–372, July 2000. doi: 10.1117/12.391526.
- Darragh O’Donoghue. Atmospheric dispersion corrector for the Southern African Large Telescope (SALT). In Richard G. Bingham and David D. Walker, editors, Large Lenses and Prisms, volume 4411 of Society of Photo-Optical Instrumentation Engineers (SPIE) Conference Series, pages 79–84, February 2002. doi: 10.1117/12.454874.
- Ferdinando Patat and Martino Romaniello. Error Analysis for Dual-Beam Optical Linear Polarimetry. PASP, 118(839):146–161, January 2006. doi: 10.1086/497581.
- Alba Peinado, Angel Lizana, Josep Vidal, Claudio Iemmi, and Juan Campos. Optimization and performance criteria of a stokes polarimeter based on two variable retarders. Opt. Express, 18(10):9815–9830, May 2010. doi: 10.1364/OE.18.009815. URL <https://opg.optica.org/oe/abstract.cfm?URI=oe-18-10-9815>.
- W. H. Press, S. A. Teukolsky, W. T. Vetterling, and B. P. Flannery. Numerical Recipes 3rd Edition: The Art of Scientific Computing. Cambridge University Press, 2007. ISBN 9780521880688. URL <https://books.google.co.za/books?id=1aA0dzK3FegC>.
- J. R. Priebe. Operational form of the mueller matrices. J. Opt. Soc. Am., 59(2):176–180, Feb 1969. doi: 10.1364/JOSA.59.000176. URL <https://opg.optica.org/abstract.cfm?URI=josa-59-2-176>.

- Lawrence W. Ramsey, M. T. Adams, Thomas G. Barnes, John A. Booth, Mark E. Cornell, James R. Fowler, Niall I. Gaffney, John W. Glaspey, John M. Good, Gary J. Hill, Philip W. Kelton, Victor L. Krabbendam, L. Long, Phillip J. MacQueen, Frank B. Ray, Randall L. Ricklefs, J. Sage, Thomas A. Sebring, W. J. Spiesman, and M. Steiner. Early performance and present status of the Hobby-Eberly Telescope. In Larry M. Stepp, editor, Advanced Technology Optical/IR Telescopes VI, volume 3352 of Society of Photo-Optical Instrumentation Engineers (SPIE) Conference Series, pages 34–42, August 1998. doi: 10.1117/12.319287.
- Maria C. Simon. Wollaston prism with large split angle. Appl. Opt., 25(3):369–376, Feb 1986. doi: 10.1364/AO.25.000369. URL <https://opg.optica.org/ao/abstract.cfm?URI=ao-25-3-369>.
- G. G. Stokes. On the Composition and Resolution of Streams of Polarized Light from different Sources. Transactions of the Cambridge Philosophical Society, 9:399, January 1852.
- Stephen F. Tonkin. Practical Amateur Spectroscopy. The Patrick Moore Practical Astronomy Series. Springer London, 2013. ISBN 9781447101277. URL <https://books.google.fr/books?id=b2fgBwAAQBAJ>.
- Pieter G. van Dokkum. Cosmic-Ray Rejection by Laplacian Edge Detection. PASP, 113 (789):1420–1427, November 2001. doi: 10.1086/323894.
- L. Wang and J. C. Wheeler. Spectropolarimetry of supernovae. ARA&A, 46:433–474, September 2008. doi: 10.1146/annurev.astro.46.060407.145139.
- Marsha J. Wolf, Matthew A. Bershad, Michael P. Smith, Kurt P. Jaehnig, Jeffrey W. Percival, Joshua E. Oppor, Mark P. Mulligan, and Ron J. Koch. Laboratory performance and commissioning status of the SALT NIR integral field spectrograph. In Christopher J. Evans, Julia J. Bryant, and Kentaro Motohara, editors, Ground-based and Airborne Instrumentation for Astronomy IX, volume 12184 of Society of Photo-Optical Instrumentation Engineers (SPIE) Conference Series, page 1218407, August 2022. doi: 10.1117/12.2630242.
- William H. Wollaston. XII. A Method of Examining Refractive and Dispersive Powers, by Prismatic Reflection. Philosophical Transactions of the Royal Society of London Series I, 92:365–380, January 1802. doi: 10.1098/rstl.1802.0013.